Available online at www.sciencedirect.com

ScienceDirect

Geochimica et Cosmochimica Acta 315 (2021) 185–206

Geochimica et Cosmochimica Acta

www.elsevier.com/locate/gca

New constraints on mid-Proterozoic ocean redox from stable thallium isotope systematics of black shales

Zijian Li [a,b,*], Devon B. Cole [a,b], Sean M. Newby [c], Jeremy D. Owens [c], Brian Kendall [d], Christopher T. Reinhard [a,b]

[a] School of Earth and Atmospheric Sciences, Georgia Institute of Technology, Atlanta, GA 30332, USA
[b] NASA Interdisciplinary Consortia for Astrobiology Research (ICAR), Alternative Earths Team, Riverside, CA 92521, USA
[c] Department of Earth, Ocean, and Atmospheric Science and National High Magnet Field Laboratory, Florida State University, Tallahassee, FL 32306, USA
[d] Department of Earth and Environmental Sciences, University of Waterloo, Waterloo, Ontario N2L 3G1, Canada

Received 18 January 2021; accepted in revised form 3 September 2021; Available online 13 September 2021

Abstract

Stable thallium (Tl) isotope data from organic-rich siliciclastic sedimentary rocks have the potential to track ocean redox state on a broad scale. Here, we report new Tl isotope data from the Mesoproterozoic Velkerri Formation (Roper Group) and the Paleoproterozoic Wollogorang Formation (Tawallah Group), McArthur Basin, Northern Territory, Australia, and interpret these in the context of rhenium-osmium (Re-Os) geochronometry on the same sample suite. Previous work has shown that marine black shales from the Velkerri Formation provide evidence for closed-system Re-Os systematics, yielding a precise isochron with an age of 1361 ± 21 Ma that agrees well with independent age constraints for the unit. The isotopic composition of authigenic Tl in euxinic black shales from the upper Velkerri Formation ($\varepsilon^{205}Tl = -2.4 \pm 0.8$, 2SD) indicates that the Tl isotope composition of local seawater at 1.36 Ga was within a plausible range for Tl inputs to the ocean. Isotope mass-balance modeling of the Tl isotope system within a Monte Carlo framework suggests that the Tl isotopic composition of seawater at 1.36 Ga was homogenous on a global scale and that the burial of Mn-oxides exerted minimal isotopic leverage on the Tl isotope composition of seawater at 1.36 Ga. Taken together with existing Mo, Cr, and U isotope data from the same samples, these observations are consistent with a low-O_2 ocean-atmosphere system during this period of the Mesoproterozoic.

Previous work has shown that the Re-Os systematics of black shales from the older (1.73 Ga) Wollogorang Formation are scattered and yield an erroneously young isochron age of 1359 ± 150 Ma, which has been attributed to post-depositional hydrothermal alteration at ~1640 Ma. We observe no systematic relationship between stable Tl isotope compositions and the extent of alteration as gauged by open-system Re-Os behavior (−4.7 ± 1.4 for the upper Wollogorang Formation and −4.8 ± 0.4 for the lower Wollogorang Formation), in marked contrast to previous observations for the molybdenum (Mo) and uranium (U) isotope systems. The invariant signature of the Tl isotope data suggests the Tl isotope system was largely unperturbed during hydrothermal alteration. However, it remains difficult to definitively rule out the possibility that authigenic Tl isotope signatures have been overprinted by later localized hydrothermal fluid alteration in the Wollogorang Formation shales. These observations highlight the potential insights afforded by evaluating open-system behavior via radiogenic isotope systems together with other stable isotope tracers in efforts to reconstruct the redox landscape of Earth's oceans over time.

Keywords: Ocean oxygenation; Proterozoic redox; Manganese cycle

* Corresponding author at: School of Earth and Atmospheric Sciences, Georgia Institute of Technology, Atlanta, GA 30332, USA.
E-mail address: zijian.li@eas.gatech.edu (Z. Li).

https://doi.org/10.1016/j.gca.2021.09.006
0016-7037/

1. INTRODUCTION

Research over recent decades has dramatically expanded our knowledge of the evolutionary history of Earth's surface O_2 levels (Lyons et al., 2014). However, the redox state of the ocean interior during the Mesoproterozoic (~1.6–1.0 Ga) remains vigorously debated. The conventional view of mid-Proterozoic ocean chemistry, based on iron speciation and redox-sensitive metal enrichment data, is that it was marked by predominantly anoxic and Fe^{2+}-rich (ferruginous) conditions, with the potential for large spatiotemporal redox heterogeneity in the surface oceans and with H_2S-rich (euxinic) waters sporadically occurring at shallow depths along continental shelf environments (Scott et al., 2008; Planavsky et al., 2011; Poulton and Canfield, 2011; Boyle et al., 2013; Partin et al., 2013; Reinhard et al., 2013, 2016; Sperling et al., 2014, 2015; Gilleaudeau and Kah, 2015; Gilleaudeau et al., 2016, 2020). Pervasively reducing conditions in the Mesoproterozoic ocean interior are also supported by the Fe redox chemistry of extrusive subaqueous volcanic rocks (Stolper and Keller, 2018), and are consistent with evidence from a range of redox proxies for relatively low atmospheric and surface ocean O_2 levels. In particular, stable chromium (Cr) isotopes, cerium (Ce) anomalies, carbon isotopes, and Zn/Fe ratios suggest Mesoproterozoic atmospheric O_2 levels at or below ~1% of the present atmospheric level (PAL) (Planavsky et al., 2014; Cole et al., 2016; Liu et al., 2016; Tang et al., 2016a; Daines et al., 2017; Bellefroid et al., 2018). A reducing, Fe-rich ocean interior and relatively low ocean-atmosphere O_2 levels are mechanistically linked, and potentially reinforce one another through impacts on marine nutrient abundance (Laakso and Schrag, 2014; Derry, 2015; Reinhard et al., 2017; Ozaki et al., 2018; Guilbaud et al., 2020).

However, several studies suggest that the redox state of the ocean interior during the early Mesoproterozoic (~1.4 Ga) may have been more dynamic in time and space. For example, iron speciation data from the Kaltasy Formation, Russia indicate the possibility of oxic deep waters in some regions at ~1.4 Ga (Sperling et al., 2014), while Zhang et al. (2016) proposed that atmospheric O_2 levels exceeded ~4% PAL at 1.4 Ga based on the redox-sensitive metal data of the Xiamaling Formation (though this interpretation has been contested; Planavsky et al., 2016). Highly fractionated Cr isotopes in 1.4 Ga shales of the Shennongjia Group (Canfield et al., 2018) and I/(Ca + Mg) ratios observed in Xiamaling carbonates (Liu et al., 2020) are also consistent with atmospheric O_2 above ~1% PAL for intervals of mid-Proterozoic time. The trace-element composition of volcanogenic massive sulfide (VMS) deposits also indicates weakly oxygenated ("suboxic") conditions for at least some periods of mid-Proterozoic time (Slack et al., 2007), consistent with U isotope data and co-occurring elevated Mo, U, and Re enrichments (Kendall et al., 2009; Cox et al., 2016; Yang et al., 2017; Sheen et al., 2018), although the positive shift of $\delta^{238}U$ may not necessarily imply a shrink in anoxic seafloor coverage (see Cole et al., 2020). In any case, further constraints on the redox state of the ocean interior are critical for refining our understanding of ocean–atmosphere oxygenation during the Mesoproterozoic.

Recently, the stable thallium (Tl) isotope system has emerged as a paleoredox proxy for the deep ocean due to its sensitivity to the burial of manganese (Mn)-oxide mineral phases (hexagonal birnessite) in marine sediments, which in turn requires pervasive oxic conditions to preserve the isotopic signature (Nielsen et al., 2011; Ostrander et al., 2017, 2019, 2020; Owens et al., 2017; Them et al., 2018; Bowman et al., 2019; Owens, 2019; Fan et al., 2020; Newby et al., 2021). Modern seawater has a homogenous $\varepsilon^{205}Tl$ of -6.0 ± 0.6, 2SD ($\varepsilon^{205}Tl = ({}^{205/203}Tl_{sample}/{}^{205/203}Tl_{NIST\ 997} - 1) \times 10{,}000$, where NIST SRM 997 is the Tl standard; Rehkämper et al., 2002; Nielsen et al., 2006b; Owens et al., 2017), which is ~4 epsilon units lighter than the average $\varepsilon^{205}Tl$ of marine inputs (volcanic gases, rivers, high-temperature hydrothermal fluids, shelf sediment porewaters, and mineral aerosols; $\varepsilon^{205}Tl \sim -2$; Nielsen et al., 2005, 2006b; Baker et al., 2009). This offset is interpreted to reflect preferential removal of the heavier Tl isotope (^{205}Tl) relative to the lighter isotope ^{203}Tl via formation and burial of Mn-oxides in oxic marine sediments, since Tl adsorption onto the Mn-oxide surface is associated with a large Tl isotope fractionation from seawater of +12 to +18 epsilon units (Rehkämper et al., 2002, 2004; Nielsen et al., 2013, 2017). In comparison, the magnitudes of Tl isotope fractionations associated with the other two primary sinks, anoxic/euxinic sediments and low-temperature alteration of oceanic crust (AOC), are much smaller. The near-quantitative removal of Tl into anoxic/euxinic sediments induces negligible Tl isotope fractionation (Owens et al., 2017, 2019). The incorporation of Tl during AOC, however, imparts a negative Tl isotope fractionation (average fractionation value of −1.5; Rehkämper and Nielsen, 2004; Nielsen et al., 2006b, 2011, 2017). The three principal sinks, oxic sediments (Mn oxide-rich), anoxic/euxinic sediments, and AOC, contribute 31%, 4%, and 65% of the total marine Tl burial flux in the modern ocean, respectively (Rehkämper and Nielsen, 2004; Baker et al., 2009; Nielsen et al., 2009, 2011, 2017; Owens et al., 2017, 2019). As a result, Mn-oxide burial in marine sediments largely dictates the modern seawater Tl isotope budget relative to other removal fluxes of Tl from the ocean (see Fig. 1).

The calibration of the Tl isotope redox tracer in modern euxinic (anoxic and containing dissolved sulfide in the water column, such as the Black Sea and Cariaco Basin) and anoxic but non-euxinic (sulfidic conditions limited to sediment pore fluids, such as the Santa Barbara Basin) environments suggests that black shales deposited under these conditions have the potential to faithfully record the $\varepsilon^{205}Tl$ of overlying seawater via quantitative sequestration of aqueous Tl phases into sediments (Owens et al., 2017; Fan et al., 2020). The modern marine Tl inventory is $\sim 8.6 \times 10^{10}$ mol and the oceanic residence time of Tl is ~18.5 kyr (Flegal and Patterson, 1985; Rehkämper and Nielsen, 2004; Baker et al., 2009; Nielsen et al., 2017; Owens et al., 2017, 2019), which is longer than the ocean mixing timescale (on the order of ~1–2 kyrs). As a result, the Tl isotope composition of seawater is largely homogeneous on a global scale. Severe basin restriction and insufficient exchange with the open sea can render euxinic

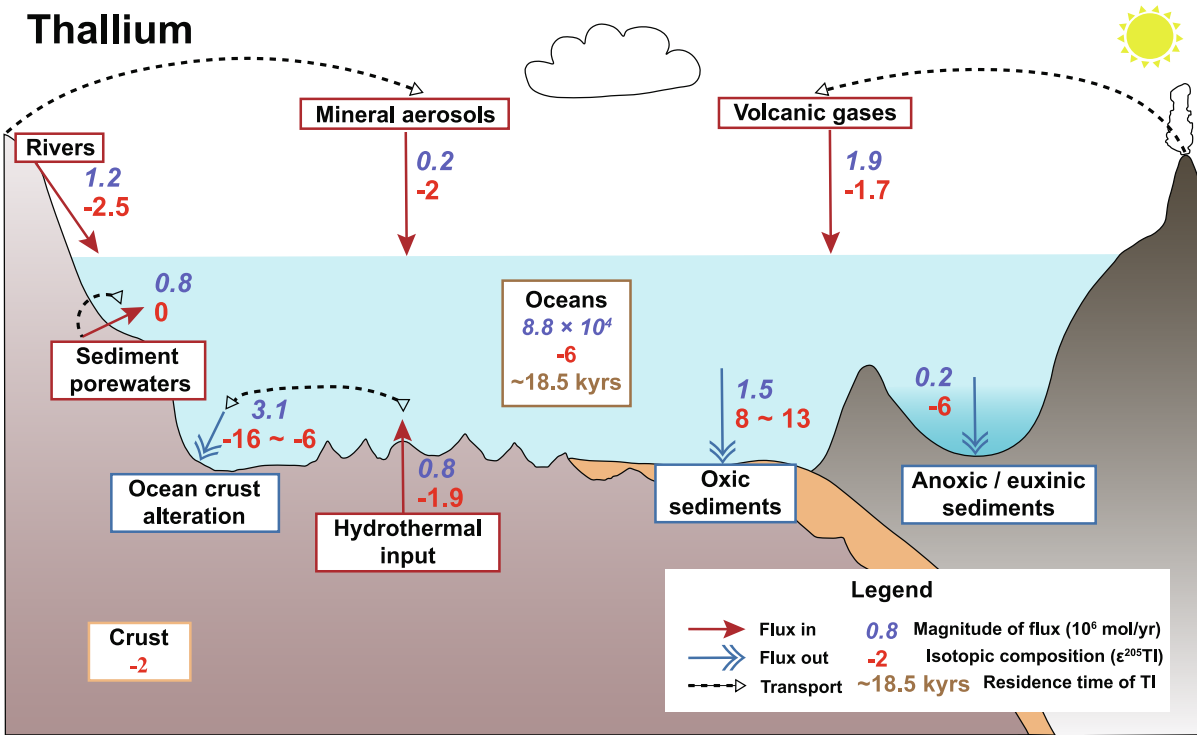

Fig. 1. Modern marine Tl isotope budget. The Tl input fluxes are denoted with red bordered rectangles and single-headed arrows, and the Tl output fluxes are represented by blue bordered boxes and double-headed arrows. The white rectangle with orange border represents "the crustal" reservoir and the white rectangle with brown border represents "the oceanic" reservoir. The Tl transport pathways are expressed by dashed arrows. The Tl isotope compositions (mean value or variation range) are labeled in red and the flux values with the unit of 10^6 mol/yr are labeled in light blue and italic font. The residence time of Tl in modern ocean is ca. 18.5 kyrs which is labeled in brown. Data are compiled from literature sources (Flegal and Patterson, 1985; Rehkämper et al., 2002, 2004; Nielsen et al., 2005, 2006b, 2009, 2011, 2017; Baker et al., 2009; Prytulak et al., 2013; Coggon et al., 2014; Owens et al., 2017; Owens, 2019; Fan et al., 2020). The base map is adapted from Little et al. (2014).

sediments unable to record the Tl isotope value of modern oxygenated open ocean waters. For instance, the Tl isotope compositions of the local water column and underlying euxinic sediments in the modern Black Sea are more positive than the open-ocean value (Owens et al., 2017). However, provided that a depositional basin is not strongly restricted from the open ocean, the Tl isotope compositions of euxinic black shales can in principle be used to constrain the ε^{205}Tl of global seawater. Accordingly, the ε^{205}Tl of ancient euxinic black shales can potentially provide insight into the redox state of the ocean interior.

In this study, we investigate the Tl isotope compositions of black shales from the ~1.4 Ga Velkerri Formation (Roper Group) that were previously analyzed for Mo, Cr, and U isotopes (Kendall et al., 2009; Cole et al., 2016; Yang et al., 2017) to provide additional constraints on the global ocean redox at ~1.4 Ga. The global burial flux of Mn-oxides in marine sediments should respond to the benthic redox landscape of Earth's oceans. One can potentially estimate the redox state of the deep ocean by leveraging the proportion of marine Tl output via manganese oxide burial, which can be derived from marine Tl isotope mass-balance modeling using the ε^{205}Tl value of contemporaneous seawater as captured in reducing organic-rich shales. In parallel, we assess the effects of post-depositional hydrothermal alteration on the Tl isotope compositions of black shales from the ~1.7 Ga Wollogorang Formation through a comparison of Tl and Re-Os isotope systematics for the same sample suite, following a similar approach previously applied to Mo and U isotope data for these samples (Kendall et al., 2009; Yang et al., 2017).

2. THALLIUM ISOTOPE PROXY

2.1. Modern oceanic Tl isotope budget

The marine Tl input and output fluxes and their Tl isotopic values in the modern ocean are summarized in Fig. 1. The Tl isotope mass balance in the modern ocean is conventionally assumed to be at steady state, with the total Tl source and sink fluxes comparable in magnitude and isotopic composition. Five major Tl oceanic inputs are considered in this study: subaerial volcanism, rivers, hydrothermal fluids, sediment porewaters from continental margins, and mineral aerosols. The estimates for oceanic Tl source fluxes and their Tl isotopic values in modern oceans are based on compilations from previous studies (Rehkämper and

Nielsen, 2004; Baker et al., 2009; Nielsen et al., 2009, 2011, 2017; Owens et al., 2017, 2019).

Subaerial volcanism is the primary input for oceanic Tl on the modern Earth, consisting of ~40% (1.8 Mmol yr^{-1}) of the total Tl input flux (Rehkämper and Nielsen, 2004; Baker et al., 2009). The average ε^{205}Tl of volcanic gases and particles is -1.7 ± 2.0 (Baker et al., 2009). The riverine dissolved flux is approximately 1.2 Mmol yr^{-1} (Rehkämper and Nielsen, 2004), constituting ~25% of the overall marine Tl source fluxes (Nielsen et al., 2017). Global rivers have an average Tl isotope composition of -2.5 ± 1.0 (Nielsen et al., 2005), which is similar to the average ε^{205}Tl of upper continental crust (Nielsen et al., 2017; Rader et al., 2018), conventionally thought to be due to limited isotope fractionation during continental weathering and riverine/estuarine transport processes (Nielsen et al., 2005). High-temperature (high-T) hydrothermal fluids leach Tl from the oceanic crust at greater depths to seawater with an annual Tl flux of 0.8 Mmol (Nielsen et al., 2006b, 2017). The mean ε^{205}Tl of high-T hydrothermal fluids is -1.9 ± 0.6 (Nielsen et al., 2006b), identical to the isotope composition of fresh MORB (Nielsen et al., 2006a). Although these oceanic Tl inputs have minor discrepancies in their Tl isotopic values, each of these Tl inputs is isotopically indistinguishable from the bulk upper continental crust (ε^{205}Tl = -2.1 ± 0.3, 2SD; Nielsen et al., 2005).

The porewaters of continental margin sediments contribute a benthic recycling Tl flux to oceans via diagenetic reduction of Mn-oxides (Rehkämper et al., 2004; Rehkämper and Nielsen, 2004). This source represents ~17% of the overall Tl input to the modern oceans, with a flux of ~0.8 Mmol yr^{-1} (Nielsen et al., 2017). The mean ε^{205}Tl of the benthic Tl flux is estimated to be ~0 (Nielsen et al., 2017) which is likely due to mixing of Tl from dissolved Mn-oxides (positive ε^{205}Tl of 6 to 12; Rehkämper et al., 2002, 2004; Nielsen et al., 2013, 2017) and Tl from seawater (negative ε^{205}Tl of ca. −6; Rehkämper et al., 2002; Nielsen et al., 2006b; Owens et al., 2017). Mineral aerosols rank as the least important oceanic Tl input to the modern oceans, with a Tl flux of 0.2 Mmol yr^{-1} (~5% of the total marine Tl source flux) and an average ε^{205}Tl of -2.0 ± 0.3 (Nielsen et al., 2005, 2017). Together, the above estimates yield an overall marine Tl input flux of ~4.8 Mmol yr^{-1} to the modern oceans with a weighted average ε^{205}Tl of −1.8 (Nielsen et al., 2017).

The fractions of marine Tl inputs during the Mesoproterozoic (targeted time interval in this study) could have been different from those in modern oceans. The riverine Tl flux at 1.4 Ga might be larger given higher modeled surface temperature and continental weathering flux (Krissansen-Totton and Catling, 2020). The higher hydrothermal heat loss in Mesoproterozoic oceans (Lowell and Keller, 2003) could also have resulted in a higher hydrothermal Tl flux. Additionally, faster continental growth rate and enhanced volcanic activities during the Mesoproterozoic compared to today (Hawkesworth et al., 2013; Dhuime et al., 2018) might lead to an elevated volcanic Tl flux. Despite the speculative higher fluxes of oceanic Tl sources at ~1.4 Ga, we would expect the ε^{205}Tl of overall marine input to be close to the modern value due to the similar chemical composition of upper continental crust since the Archean (Dhuime et al., 2015; Tang et al., 2016b) and relatively insignificant impacts on isotope mass balance from localized variability associated with continental weathering, high-T hydrothermal circulation, and volcanic outgassing (Nielsen et al., 2005, 2006b; Baker et al., 2009).

There are three primary marine Tl outputs: low-temperature alteration of oceanic crust (AOC), Mn-oxide burial in oxic sediments, and burial in anoxic/euxinic sediments (Fig. 1). The largest single Tl sink from the modern ocean is the AOC flux, estimated at ~3.1 Mmol yr^{-1}, which accounts for around 65% of the total marine Tl output (Rehkämper and Nielsen, 2004; Nielsen et al., 2017). The altered upper oceanic crust has an average ε^{205}Tl of ~−7.5 with an isotopic range between −16 and −6 (Nielsen et al., 2006b; Prytulak et al., 2013; Coggon et al., 2014). The Tl isotopic fractionation of AOC ($\Delta^{205}Tl_{AOC\text{-}sw}$) thus has a mean of −1.5 ε-units due to the small isotope fractionation during the final removal of Tl via deeper oceanic crust (Nielsen et al., 2017; Owens, 2019).

Burial in association with Mn-oxides requires oxic sediments, which constitute the second largest marine Tl sink in the modern ocean, with an estimated flux of 1.5 Mmol yr^{-1} or ~32% of the total output Tl flux (Rehkämper and Nielsen, 2004; Nielsen et al., 2017). The average Tl isotope composition of Mn-oxides is ~+10 (ranging from +6 to +13), which yields a mean fractionation value from seawater ($\Delta^{205}Tl_{MnOx\text{-}sw}$) of +16 with the lower and upper bounds of +14 and +19, respectively (Rehkämper et al., 2002, 2004; Nielsen et al., 2009, 2013, 2017). The preferential scavenging and retention of the heavy Tl isotopes (^{205}Tl) by Mn-oxides is ascribed to oxidation of aqueous Tl(I) to surface-complexed Tl(III) during adsorption onto low-temperature Mn-oxide, specifically hexagonal birnessite (Bidoglio et al., 1993; Peacock and Moon, 2012; Nielsen et al., 2013).

The remaining significant Tl sink in the modern ocean is anoxic/euxinic sediments, which currently account for roughly 4% of the total oceanic Tl output (Owens, 2019). Due to (near) quantitative Tl removal in such settings, there is currently thought to be negligible isotopic fractionation associated with burial into anoxic/euxinic sediments ($\Delta^{205}Tl_{Eux\text{-}sw} = 0$; Owens et al., 2017; Fan et al., 2020). The overall marine Tl sink flux is thus ~4.8 Mmol yr^{-1} with a weighted average ε^{205}Tl of −1.8 (Nielsen et al., 2017).

2.2. Extracting a global seawater ε^{205}Tl value from sedimentary records

Authigenic sulfide phases hosted in black shales deposited under locally euxinic conditions have been proposed to record the Tl isotopic composition of contemporaneous bottom waters (Nielsen et al., 2011; Ostrander et al., 2017, 2019, 2020; Them et al., 2018; Bowman et al., 2019; Fan et al., 2020). Observations from the Cariaco basin and the Black Sea find that deep waters near the sediment–water interface are almost entirely devoid of Tl (Owens et al., 2017). In addition, the ε^{205}Tl of sediments and oxic seawater in the Cariaco Basin are -5.1 ± 1.3 (2SD) and -5.5 ± 0.7

(2SD), respectively, and the ε^{205}Tl of the counterparts in the Black Sea are −2.3 ± 0.6 (2SD) and −2.2 ± 0.3 (2SD), respectively, suggesting the ε^{205}Tl of authigenic (likely pyrite-hosted) Tl leached from organic-rich sediments within both euxinic basins is identical to that of the overlying water column (Owens et al., 2017). Sediments deposited in sulfidic pore fluids beneath a low-O_2 water column in the Santa Barbara Basin (ε^{205}Tl = −5.6 ± 0.1, 2SD; Fan et al., 2020) also appear to faithfully capture the Tl isotope values of global seawater (−6.0 ± 0.6, 2SD; Rehkämper et al., 2002; Nielsen et al., 2006b; Owens et al., 2017). These observations suggest that dissolved Tl is nearly quantitatively removed from the water column and sequestered in authigenic pyrite when free sulfide is present in either water column or pore fluids, which should minimize any Tl isotopic fractionation associated with sequestration into a solid phase under reducing conditions.

However, there are no observations to date to evaluate whether Tl isotopic fractionation can occur under ferruginous conditions under relatively low sulfate concentrations and thus a low potential for abundant free sulfide. Indeed, existing observations of Tl concentration and ε^{205}Tl through the chemocline of the Black Sea imply a negative Tl isotope fractionation during Tl incorporation into pyrite (^{203}Tl preferentially concentrates in pyrite). The associated isotope fractionation ($\Delta^{205}Tl_{py\text{-}sw}$) is estimated to be between −3 and −1 (Owens et al., 2017). In this scenario, the incomplete removal of Tl into small amounts of authigenic pyrite in ferruginous and/or weakly sulfidic systems would be expected to record Tl isotopic values in sediments that are ^{203}Tl-enriched relative to overlying seawater. The Santa Barbara Basin is the closest modern analog measured to date, but there are significant differences between sulfate availability and dissolved Fe in this system relative to truly ferruginous environments. However, a recent study shows that the euxinic shales deposited during the Ediacaran Period from South China (not including negative excursions thought to capture times of more severe basin restriction) have indistinguishable Tl isotopic values (ε^{205}Tl = −2.1 ± 0.6, 2SD) compared to broadly coeval ferruginous shales from northwestern Canada (ε^{205}Tl = −2.1 ± 0.3, 2SD), which is interpreted in both cases to capture the ε^{205}Tl of overlying seawater at the time of sediment deposition (Ostrander et al., 2020). In any case, although there is currently no firm evidence from modern anoxic and non-sulfidic settings that such environments significantly fractionate Tl isotopes relative to water column values, the most conservative approach at present is to consider stable Tl isotope compositions of ferruginous shales a lower bound on coeval seawater, while utilizing clearly and persistently sulfidic and euxinic systems as the most robust archive of contemporaneous water column isotope compositions.

Another key factor to consider in attempts to reconstruct ancient seawater ε^{205}Tl is basin restriction. Analysis of seawater samples in the southern Atlantic Ocean (collected from the UK GEOTRACES 40°S cruise) suggests that the Tl isotope composition of modern open ocean water is homogenous, with an overall average of −6.0 ± 0.6, 2SD (Rehkämper et al., 2002; Nielsen et al., 2006b; Owens et al., 2017). If a local depositional basin is well-connected to the open ocean, the ε^{205}Tl of seawater in the local basin is likely to match that of open ocean waters provided the residence time of Tl in the ocean (modern value of ca. 18.5 kyr) is sufficiently longer than the modern ocean mixing timescale. Modern seawater in the Cariaco Basin has an ε^{205}Tl of −5.5 ± 0.7, 2SD (Owens et al., 2017), indistinguishable from the global ocean value (−6.0 ± 0.6, 2SD), implying that even silled and semi-restricted basins can reflect the Tl isotope signature of the open ocean. However, if the basin is more strongly restricted, the Tl isotope composition of the local basin may deviate from global seawater due to the local influence of Tl sources and sinks within the basin. A striking example of this is provided by the Black Sea, in which the ε^{205}Tl of surface seawater is −2.2 ± 0.3 (2SD), reflecting a basinal mass balance dominated by continental runoff input (ε^{205}Tl = −2.5 ± 1.0, 2SD; Nielsen et al., 2005) and the lack of a significant oxic sink (Owens et al., 2017).

3. SAMPLE DESCRIPTION AND BACKGROUND

3.1. Velkerri Formation

Black shale samples of the Velkerri Formation were collected from the Urapunga-4 drill core from the McArthur Basin in Northern Territory, Australia (Kendall et al., 2009; Fig. 2). The Velkerri Formation belongs to the Roper Group (Roper Superbasin) and is sandwiched between the overlying McMinn Formation and the underlying Corcoran Formation (Fig. 3). The Velkerri Formation has a thickness of ~900 m (Ahmad and Dunster, 2013), with facies dominated by organic-rich black shale and minor deposition of glauconitic siltstone and sandstone (Jackson and Raiswell, 1991; Warren et al., 1998; Abbott and Sweet, 2000). It is worth noting that in our study we only target thin intervals of black shales in the drill core Urapunga-4 with a total thickness of ~2 m (~137–138 m and ~326–327 m; the same sample suite used in Kendall et al. (2009) and Yang et al. (2017)), which capture very brief episodes of Velkerri Formation deposition (Fig. 3). This sampling scheme was originally employed by Kendall et al. (2009) to ensure a uniform initial $^{187/188}$Os value across samples, which is essential for implementation of the Re-Os isochron technique for black shale geochronology. The Velkerri Formation is organic-carbon rich, with TOC contents up to 9 wt% (Crick et al., 1988; Jackson and Raiswell, 1991; Warren et al., 1998; Cox et al., 2016; Mukherjee and Large, 2016), and is interpreted to have been deposited in a low-energy shelf setting (Abbott and Sweet, 2000). Previous chemostratigraphic studies indicate that the Roper Group epeiric seaway was at least partially connected to the open ocean (Jackson and Raiswell, 1991; Warren et al., 1998; Abbott and Sweet, 2000; Shen et al., 2003; Johnston et al., 2008; Cox et al., 2016; Mukherjee and Large, 2016; Yang et al., 2018), with water column chemistry oscillating between anoxic and Fe-rich (ferruginous) and euxinic conditions (Kendall et al., 2009; Cox et al., 2016; Mukherjee and Large, 2016). The Re-Os depositional ages of the two intervals studied here (the

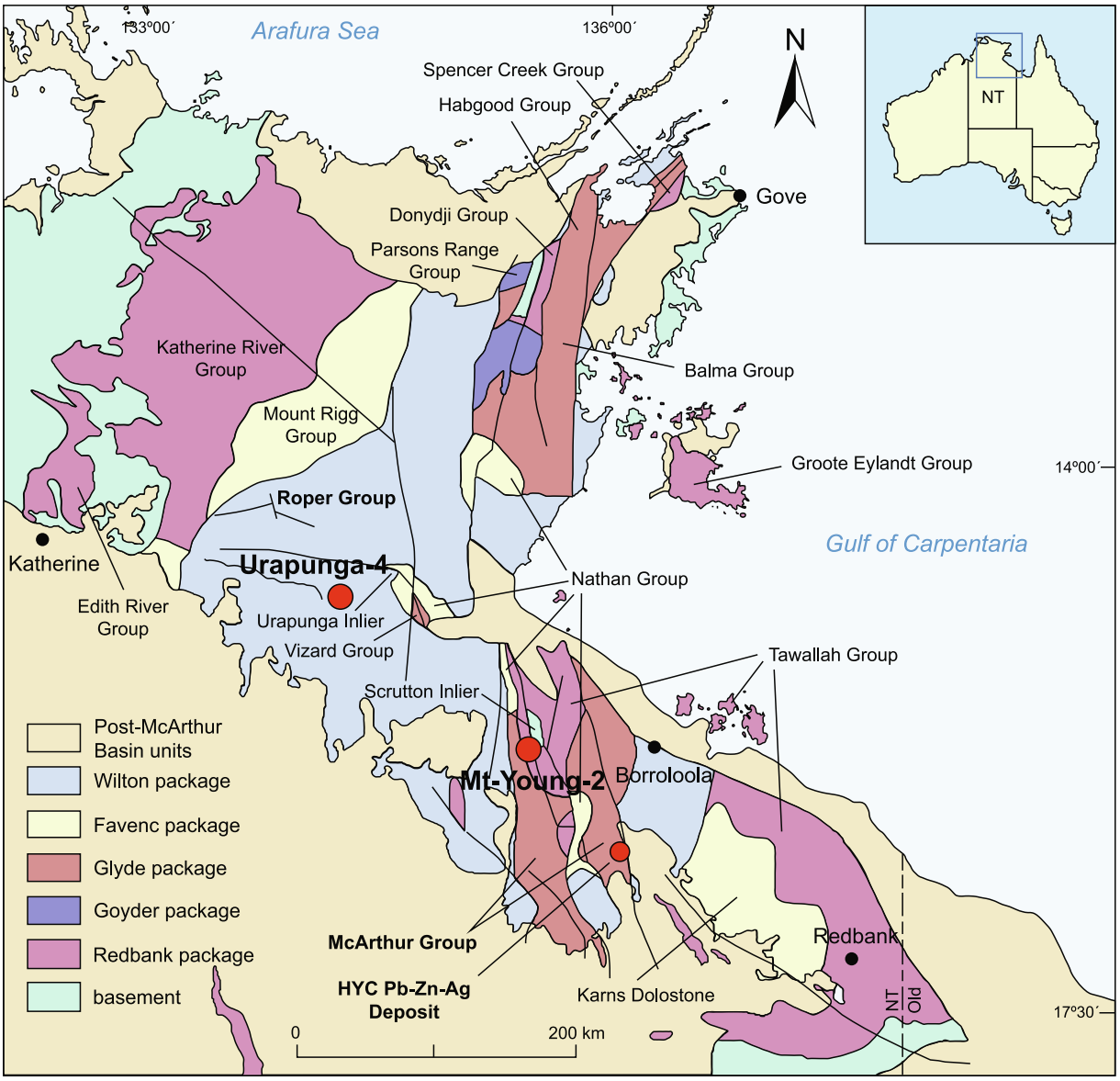

Fig. 2. Regional geologic map of the McArthur Basin, Northern Territory, Australia. The locations of the drill core Urapunga-4 (Velkerri Formation) of Roper Group, the drill core Mt-Young-2 (Wollogorang Formation) of McArthur Group, and the McArthur River (HYC) Pb-Zn-Ag ore deposit are labeled with red circles. Modified from Volk et al. (2005), Kendall et al. (2009), Mukherjee and Large (2016), and Yang et al. (2017).

upper Velkerri Formation, between ~137–138 m, and the lower Velkerri Formation, between ~326–327 m) are 1361 ± 21 Ma and 1417 ± 29 Ma, respectively (Kendall et al., 2009). The Re-Os isochron ages are verified by the youngest detrital zircon U-Pb age of 1308 ± 41 Ma for the fine-grained siltstone from the upper Velkerri Formation (Yang et al., 2018, 2019) as well as a U-Pb baddeleyite age of 1327.5 ± 0.6 Ma for the Derim Derim Dolerite that intrudes the entire Velkerri Formation and overlying units in the upper Roper Group (Bodorkos et al., 2021).

The two intervals of the Velkerri Formation show distinct chemostratigraphic signatures (Kendall et al., 2009). The upper Velkerri interval (~137–138 m) is characterized by high degrees of pyritization (DOP), generally DOP of ~0.9, with elevated Fe_T/Al ratios of 1.4–1.8 (Kendall et al., 2009). Pronounced Mo enrichments (106–119 ppm), together with elevated DOP and strong Fe enrichment, suggest a persistently euxinic depositional environment. In contrast, the lower Velkerri interval (~326–327 m) displays lower DOP values (0.43–0.51), generally lower but sporadically elevated Fe_T/Al ratios (0.5–1.4), and subtle Mo enrichment (6–9 ppm), all of which are consistent with deposition under ferruginous conditions.

Only the upper Velkerri Formation interval (~137–138 m) has been analyzed for Mo isotope compositions (Arnold et al., 2004; Kendall et al., 2009). The average

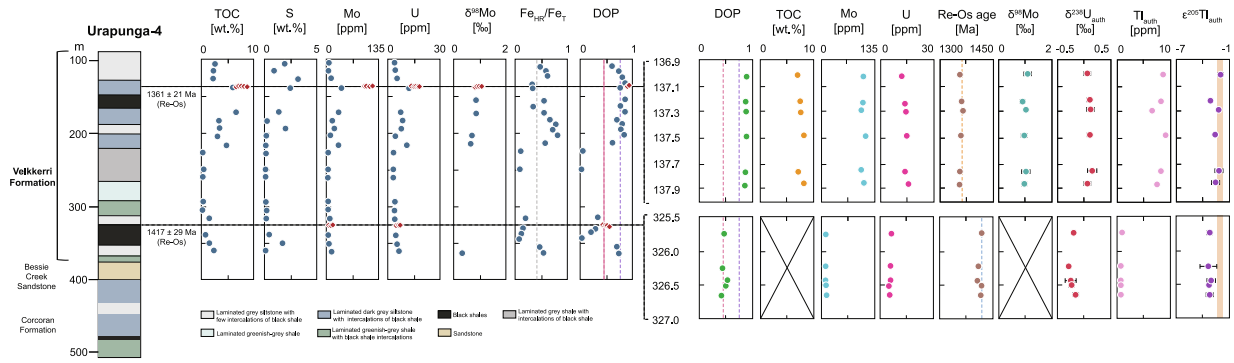

Fig. 3. Chemostratigraphic profiles for the Velkerri Formation (drill hole Urapunga-4). The geochemical data of the entire Velkerri Formation are shown in the left chemostratigraphic columns which are labeled with cyan circles, and the geochemical data of the samples in this study (Re-Os dated intervals) are labeled with magenta diamonds. Re-Os depositional ages of upper and lower Velkerri Formation are from Kendall et al. (2009). The TOC, S, Mo, U data are from Kendall et al. (2009), Mukherjee and Large (2016), and Yang et al. (2017); the δ^{98}Mo data are from Arnold et al. (2004) and Kendall et al. (2009); the Fe_{HR}/Fe_T and DOP data are from Shen et al. (2003). The grey dashed line at Fe_{HR}/Fe_T value of 0.38 is the boundary between anoxic and oxic conditions. The pink dashed line at DOP value of 0.45 is also the boundary between anoxic and oxic. The DOP value at 0.75 represents the boundary between anoxic and euxinic conditions (Raiswell and Canfield, 1998; Lyons and Severmann, 2006), which is denoted as the purple dashed line. The geochemical data of the samples in the upper (136.9–137.9 m) and lower (325.71–326.69 m) Velkerri Formation intervals are shown in the right chemostratigraphic columns. No TOC and Mo isotope data exist for the lower Velkerri Formation interval. The Re-Os ages of individual samples are calculated in this study by using the Re-Os isotope data reported in Kendall et al. (2009). The orange and blue dashed lines in the Re-Os age columns denote the Re-Os dating ages of the two sampled intervals, 1361 Ma and 1417 Ma, respectively, as reported by Kendall et al. (2009). The δ^{238}U data are from Yang et al. (2017). The Tl concentration and ε^{205}Tl data for the authigenic fraction of the samples are from this study. The tan shaded bar in the ε^{205}Tl columns denotes the Tl isotopic values for the bulk upper continental crust ($\varepsilon^{205}Tl = -2.1 \pm 0.3$, 2SD; Nielsen et al., 2005). Data are reported in Table 1 and S1-2. The stratigraphic column is adapted from Mukherjee and Large (2016) and Yang et al. (2017).

reported $\delta^{97/95}$Mo value of 0.72 ± 0.10‰ (2SD) is equivalent to a δ^{98}Mo value of 0.95 ± 0.14‰ (2SD) relative to standard NIST SRM 3134 (δ^{98}Mo = 0.25‰; Nägler et al., 2013). Combined Mo-U isotope mass balance modeling tentatively suggested the estimated δ^{98}Mo of coeval seawater during the deposition of the upper Velkerri Formation was at least 1.50‰ (1.50–2.23‰; Lu et al., 2020). In this light, the observed δ^{98}Mo value, as well as Mo concentration data (Reinhard et al., 2013), implies that roughly ~2% of the seafloor was overlain by strongly sulfidic waters at 1.36 Ga as opposed to ~0.1% euxinic seafloor coverage in the modern oceans (Reinhard et al., 2013).

The average uranium isotope values for the authigenic fraction ($\delta^{238}U_{auth}$) of the upper and lower Velkerri Formation intervals are 0.13 ± 0.04‰ (1SD) and −0.08 ± 0.18‰ (1SD), respectively (Yang et al., 2017). Using a coupled Mo-U isotope mass balance model, the average δ^{238}U value of contemporaneous seawater during deposition of the upper Velkerri Formation was calculated to be −0.70‰ to −0.34‰ (Lu et al., 2020). The δ^{238}U of coeval seawater during the deposition of the lower Velkerri interval was originally estimated to be −0.68‰ to −0.93‰ by assuming $\Delta^{238}U_{sed\text{-}SW}$ was 0.60–0.85‰ (Yang et al., 2017). However, this suggested value is difficult to validate given recent observations of highly variable U isotope fractionation in ferruginous settings (Cole et al., 2020). Nevertheless, the U isotope data can be re-interpreted to indicate expanded euxinic conditions during the upper Velkerri interval, and relatively less extensive euxinic conditions during the lower Velkerri interval. Expanded euxinia during deposition of the upper Velkerri interval may reflect a period of greater sulfate input and possibly also enhanced deep ocean oxygenation (increased marine sulfate concentrations suggested from sulfur isotope data; Shen et al., 2003; Yang et al., 2017). Despite this possible transient pulse of expanded euxinia, the U isotope mass balance model suggests that the euxinic coverage was no more than ~7% of the global seafloor during the Mesoproterozoic (Gilleaudeau et al., 2019).

The chromium isotope (δ^{53}Cr) compositions of the upper and lower Velkerri Formation intervals are −0.14‰ to + 0.05‰ and −0.14‰ to −0.09‰ (relative to NIST SRM 979), respectively (Cole et al., 2016). The δ^{53}Cr values of the two intervals are extremely homogeneous and are indistinguishable from the bulk silicate Earth (BSE) (Schoenberg et al., 2008; Cole et al., 2016), suggesting that atmospheric O_2 at 1.36 Ga was below the level necessary to trigger extensive oxidative weathering and redox cycling of Cr in terrestrial and coastal marine settings (Planavsky et al., 2014; Cole et al., 2016).

3.2. Wollogorang Formation

Black shales from the Wollogorang Formation were collected from the Mount Young 2 drill core of the McArthur Basin in Northern Territory, Australia (Kendall et al., 2009; Fig. 2). The Wollogorang Formation belongs to the Tawallah Group (Calvert Superbasin) which is bracketed by the overlying Gold Creek Volcanics and the underlying Settlement Creek Volcanics (Cooke et al., 2000; Fig. 4). The Wollogorang Formation has a thickness of ~100–150 m (Ahmad and Dunster, 2013), with facies dominated by

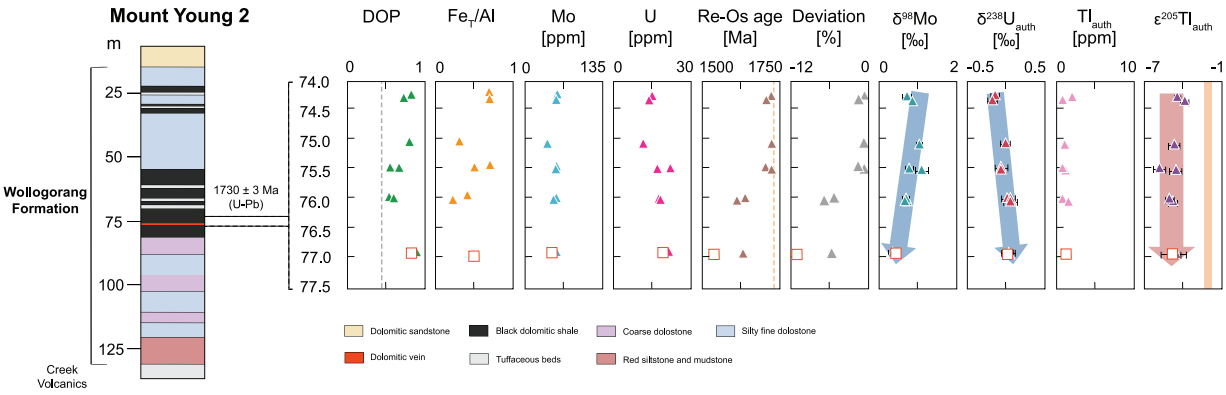

Fig. 4. Chemostratigraphic profiles for the samples of the Wollogorang Formation (drill hole Mount Young 2) in this study (Re-Os dated intervals). SHRIMP U-Pb zircon ages of tuffaceous beds are from Page et al. (2000). The DOP, Fe_T/Al, Mo concentration and $\delta^{98}Mo$ data are from Kendall et al. (2009). The U concentration and $\delta^{238}U_{auth}$ data are from Yang et al. (2017). The Re-Os age and percent deviation data for individual samples are calculated in this study by using the Re-Os isotope data reported in Kendall et al. (2009). The orange dashed lines in the Re-Os age column denotes the reference Re-Os isochron age of 1730 Ma (Kendall et al., 2009). The Tl concentration and $\varepsilon^{205}Tl$ data for the authigenic fraction of the samples are from this study. The grey dashed line in the DOP column represents the value of 0.45, indicating the boundary between anoxic and oxic conditions. The open red squares denote the data of the black shale sample (76.91–76.96 dol) adjacent to a dolomitic vein. The tan shaded bar in the $\varepsilon^{205}Tl$ column represents the Tl isotopic values for the bulk upper continental crust ($\varepsilon^{205}Tl = -2.1 \pm 0.3$, 2SD; Nielsen et al., 2005). Data are reported in Table 1 and S1-2. The stratigraphic column is adapted from Mukherjee and Large (2016) and Yang et al. (2017).

dolomitic sandstone, siltstone, and mudstone and with deposition of dolomitic organic-rich black shale as well as dolostone (Jackson, 1985; Donnelly and Jackson, 1988). Similar to the sampling resolution for the Velkerri Formation, we only focus on samples from a ~3 m interval (~74–77 m depth in drill core Mount Young 2) of black shales in the Wollogorang Formation that were originally targeted for Re-Os isotope analyses by Kendall et al. (2009) and also analyzed for Mo and U isotope compositions by Kendall et al. (2009) and Yang et al. (2017), respectively. This sediment interval belongs to the maximum flooding surface in the middle Wollogorang Formation (characterized as 'ovoid beds' in lithofacies analysis) and spanned offshore (below storm-wave base) hemipelagic and/or low-density turbidity current depositional settings (Kunzmann et al., 2020). The pyritic black shale unit (~20–25 m thick) containing the sampled interval has an average TOC content of ~6 wt.% and contains dolomitic nodules and veins (Donnelly and Jackson, 1988; Kendall et al., 2009; Spinks et al., 2016; Kunzmann et al., 2020). Existing lithofacies characterization and chemostratigraphic data (Mo enrichments, Fe speciation, DOP values, and sulfur (S) isotopes) suggest that the Wollogorang sediments were stratigraphically homogenous and deposited on a large epeiric platform without much topography (Kunzmann et al., 2020). The bottom waters were periodically euxinic and the basin connection to the open ocean was semi-restricted from time to time (Jackson et al., 2000; Page et al., 2000; Southgate et al., 2000; Shen, 2002; Kendall et al., 2009; Spinks et al., 2016).

The southern McArthur Basin is host to world-class Pb-Zn-Ag deposits, including the McArthur River (HYC) and Teena deposits, hosted by the ca. 1640 Ma Barney Creek Formation (Fig. 2). The associated ore fluids are estimated to be oxidized (HSO_4^- predominant), acidic (pH below 4), and low-salinity brines (~15 wt% NaCl equiv.) with the temperature around 150 °C (Cooke et al., 2000). Such saline mineralizing fluids transported Zn, Fe, and Tl (leached from the Settlement Creek and Gold Creek Volcanics in the Upper Tawallah Group; Cooke et al., 1998) until reduction by the pyritic-carbonaceous sediments of the Barney Creek Formation to precipitate sphalerite and proximal Tl-rich diagenetic pyrite, in association with replacement (acid dissolution) of dolomite (Spinks et al., 2021). The report of indigenous biomarkers, low T_{max} values, and lack of signs of alteration in many drill cores of the Wollogorang Formation suggest that, overall, the Wollogorang sediments did not pass the oil window and remained pristine across the entire basin (Kunzmann et al., 2020; Vinnichenko et al., 2020). However, some sections of the Wollogorang Formation (e.g. drill core Mount Young 2) show signs of localized hydrothermal overprinting (copper sulfides enrichment, elevated abundances in Zn, Pb, and Tl, and periodically-high concentrations of pyrite deposition) and up to sub-greenschist thermal metamorphism (Jackson, 1985; Southgate et al., 2000; Spinks et al., 2016). These geochemical signatures, together with evidence from paleomagnetism (overprinting of paleomagnetic poles; Idnurm et al., 1995; Idnurm, 2000; Symons, 2007) and petrology (large pyrite aggregates and dolomitic veinlets; Jackson, 1985; Donnelly and Jackson, 1988), suggest that the localized post-depositional alteration of the Wollogorang Formation was closely relevant to the ca. 1640 Ma mineralization event that formed the giant McArthur River HYC deposit (Crick et al., 1988; Donnelly and Jackson, 1988; Idnurm et al., 1995, 2000; Cooke et al., 1998; Jackson et al., 2000; Garven et al., 2001; Logan et al.,

2001; Rawlings et al., 2004; Williford et al., 2011). The local hydrothermal alteration of the Wollogorang Formation in Mount Young 2 might be ascribed to the drill core location close to a basement inlier faulted contact with the Paleoproterozoic strata from which fluid flow probably percolated (Fig. 2). The hydrothermal fluids that altered the Wollogorang Formation shales are speculated to share some physiochemical properties in common with the mineralizing brines of the HYC SEDEX deposit (Spinks et al., 2016). In particular, the alteration fluids that moved through the Wollogorang black shales in Mount Young 2 are estimated to have low-to-moderate temperatures (~100–200 °C) and are enriched in base metals by analogy with the ore fluids that shaped the McArthur River HYC deposit (Southgate et al., 2000; Polito et al., 2006).

Although lowermost greenschist facies metamorphism is conventionally assumed not to perturb the Re-Os geochronometer (Kendall et al., 2004; Rooney et al., 2011), the post-depositional hydrothermal event at around 1640 Ma was found to disturb the Re-Os isotope systematics of black shales of the Wollogorang Formation in the studied drill core (Kendall et al., 2009). Re-Os dating of black shales in the ~74–77 m interval of the Mount Young 2 drill core yields an erroneous age of 1359 ± 150 Ma with a strongly discordant errorchron (Kendall et al., 2009), notably younger than the SHRIMP U-Pb zircon ages of 1729 ± 4 Ma and 1730 ± 3 Ma, dated from the tuffaceous beds a few meters above the interval targeted for Re-Os isotope analysis (Page et al., 2000). The initial $^{187}Os/^{188}Os$ value of the Wollogorang shales (I_{Os}) derived from the isochron regression is 3.5 ± 1.5 which is significantly higher than the Os isotope composition of the most radiogenic reservoirs on present-day Earth (~1.0 to 1.4 for upper continental crust; Esser and Turekian, 1993; Peucker-Ehrenbrink and Hannigan, 2000; Hattori et al., 2003; Chen et al., 2016). Considering less radiogenic ^{187}Os accumulated during the Paleoproterozoic compared to today, the $^{187}Os/^{188}Os$ of the Paleoproterozoic upper continental crust would have been lower (Yang et al., 2017). Since Os and Re in reducing environments primarily concentrate in organic matter (Ravizza et al., 1991; Ravizza and Esser, 1993; Martin et al., 2000; Peucker-Ehrenbrink and Hannigan, 2000; Creaser et al., 2002; Jaffe et al., 2002; Selby and Creaser, 2003) and authigenic sulfides (Miller et al., 2011; Helz and Dolor, 2012), the erroneous Re-Os isochron age and the abnormally high I_{Os} value are readily explained by the differential remobilization of Re and Os during disturbance of organic matter and sulfides via post-depositional fluid flow. The bottom of the studied interval (~76–77 m) in the Wollogorang Formation appears to have undergone the most intense alteration, as evidenced by a higher initial $^{187}Os/^{188}Os$ ratio from an isochron regression of this sub-interval (4.8 ± 4.3) and the most severe deviation from a ~1730 Ma reference Re-Os isochron (Kendall et al., 2009; Fig. 4). These signatures indicate migration of the hydrothermal fluids from (stratigraphic) bottom to top through the sequence.

The $\delta^{98}Mo$ values (relative to NIST SRM 3134 = 0.25 ‰) of the Wollogorang Formation sampled from the same ~74–77 m core depth interval range between 0.30‰ and 1.03‰ with the lightest Mo isotope value (0.30‰) occurring at the bottom of the interval. This implies addition of Mo from an oxidizing fluid, which can favor isotopically light Mo being added, or otherwise, heavier Mo isotopes were preferentially leached out of the black shales (Kendall et al., 2009). The U isotope values of the authigenic fraction ($\delta^{238}U_{auth}$) of the upper section (74.27–75.53 m) and lower section (76.00–76.96 m) in the same interval of the Wollogorang Formation are −0.04 ± 0.09‰ (1SD) and 0.10 ± 0.05‰ (1SD), respectively (Yang et al., 2017), suggesting that either ^{238}U from hydrothermal fluids was preferentially added to the black shales during reductive U sequestration or the lighter U isotope (^{235}U) was preferentially leached from the shales during fluid-rock interaction.

4. METHODS

4.1. Leaching and dissolution procedure

The authigenic leaching and digestion were conducted under trace metal-clean conditions at Georgia Institute of Technology and in the National High Magnetic Field Laboratory (NHMFL) at Florida State University, following the procedures described in Nielsen et al. (2011) and Owens et al. (2017). Around 150 mg of 200-mesh sample powder was treated with 3 ml of 2 M HNO_3 and heated on a hotplate at 130 °C for 12 hours. The supernatant was extracted to separate authigenic Tl from detrital Tl. To dissolve suspended organic matter, dried supernatants were further reacted with 3 ml of a 50:50 (v/v) mixture of concentrated HNO_3-HCl acid, heated at 120 °C overnight, and then transferred to a CEM Mars 6 microwave for 4 hours. An extra 1 ml of 50% HNO_3 and ~100 µl of pure trace metal grade H_2O_2 was added to dried samples to ensure the dissolution of all organic matter. A few drops of concentrated HCl were added to dried samples and immediately dried down. The samples were reconstituted with 1 ml of 1 M HCl and treated with 100 µl of brominated H_2O in preparation for Tl column chemistry. The acids used during leaching and dissolution steps were Aristar/trace-metal grade. The USGS reference material SCo-1 (Cody Shale) and a procedural blank were prepared together with natural samples during sample preparation to monitor external reproducibility.

4.2. Tl isotope and concentration analysis

Thallium isotope analysis was conducted at the NHMFL. The complete separation of Tl from the sample matrix was achieved via ion-exchange chromatography developed by Rehkämper and Halliday (1999) and Nielsen et al. (2004). Pre-cleaned micro PFA columns were loaded with approximately 100 µl of 200–400 mesh Bio-Rad AG1-X8 anion exchange resin (rinsed with weak acid and MQ water several times before loading). The loaded columns were eluted with an excess of three column volumes of 0.1 M HCl-SO_2 and 0.1 M HCl separately to wash the resin. The resin was conditioned with 0.1 M HCl-1% Br_2-H_2O (the volume percent of 0.1 M HCl and saturated bromine water is 99% and 1%, respec-

tively) prior to loading samples prepared from previous leaching and dissolution steps, including standards and blanks. Matrix elements, especially the major potential isobaric interference lead (Pb), were eluted from the columns with 1.8 ml of 0.5 M HNO_3-3% Br_2-H_2O, 1.6 ml of 2 M HNO_3-3% Br_2-H_2O, and 1.6 ml of 0.1 M HCl-1% Br_2-H_2O. Thallium was then collected via the elution of 1.6 ml of 0.1 M HCl-SO_2 through the columns, then the samples were evaporated on a hotplate at 120 °C. When samples were approaching dryness, the temperature of the hotplate was adjusted to ~210 °C for approximately two hours until dryness. Samples were then reconstituted with 50 µl of 50:50 (v/v) HNO_3-HCl, capped, and placed on a 120 °C hotplate for approximately three hours. Beakers were uncapped and the samples were evaporated on a hotplate to dryness. Dried samples were reconstituted in 50 µl of concentrated HNO_3 and dried down again on a hotplate at 120 °C. Finally, 500 µl of 0.1 M HNO_3-0.1% H_2SO_4 was added to the beakers for the preparation of Tl isotope analysis. All the acids used in the column chemistry were double-distilled and clean Teflon beakers were used for each step. The recovery of Tl after column chemistry is within analytical error of 100%, as verified by the earlier work which yielded the constant replication of USGS shale standard SDO-1 (average ε^{205}Tl of -2.0 ± 0.3, 2SD).

The Tl isotope compositions of purified samples were measured with a Thermo Fisher Neptune multi-collector inductively coupled plasma mass spectrometer (MC-ICP-MS) operated in low-resolution mode at the NHMFL following the established analytical methods (Rehkämper and Halliday, 1999; Nielsen et al., 2004). The Tl isotope analysis utilized external normalization to NIST SRM 981 Pb with standard-sample bracketing (the bracketing Tl standard is NIST SRM 997) to correct for instrumental mass bias (Rehkämper et al., 2002; Nielsen et al., 2004, 2009, 2011; Baker et al., 2009). With addition of a known quantity of NIST SRM 981 Pb, the Tl concentrations were determined via converting from the measured ^{205}Tl/^{208}Pb ratios during the isotopic analysis. The precision and accuracy of Tl concentration and isotope analysis at the NHMFL is monitored via routinely analyzing USGS shale standard SCo-1. The analysis of the authigenic fraction of SCo-1 yielded results for Tl concentration of 205 ± 36 ppb (2SD, n = 3), consistent with previously reported value of 213 ± 79 ppb (2SD) (Ostrander et al., 2017; Owens et al., 2017; Fan et al., 2020) within analytical error of ± 6%. Procedural blanks were below the detection limit for Tl (<5 pg) which is insignificant (<0.1%) compared to the amounts of sample Tl analyzed. The Tl isotope compositions (ε^{205}Tl) of standards and samples are reported as per epsilon deviation from the NIST 997 standard as follows: $\varepsilon^{205}\text{Tl} = (^{205/203}\text{Tl}_{\text{sample}}/^{205/203}\text{Tl}_{\text{NIST 997}} - 1) \times 10{,}000$. The analysis of SCo-1 in this study yielded Tl isotope values of -3.0 ± 0.2 (2SD, n = 6) which is within the uncertainty of the long-term value of SCo-1 of -3.0 ± 0.3 (2SD) (Ostrander et al., 2017, 2019, 2020; Owens et al., 2017, 2019; Them et al., 2018; Bowman et al., 2019; Fan et al., 2020).

5. RESULTS

Authigenic Tl concentrations of black shales within both the upper (136.9–137.9 m) and lower (325.5–327.0 m) Velkerri Formation are relatively invariant, however, the Tl_{auth} abundances of the upper Velkerri interval (8.07 ± 0.36 ppm SE; Table 1; Fig. 3) are about an order of magnitude higher than the Tl_{auth} abundances of the lower Velkerri interval (0.62 ± 0.09 ppm SE; Table 1; Fig. 3). Black shales from the upper Velkerri Formation have an average $\varepsilon^{205}\text{Tl}_{\text{auth}}$ of -2.4 ± 0.8 (2SD; Table 1; Fig. 3). The authigenic Tl isotope compositions from the lower Velkerri Formation yield an average value of -3.3 ± 0.4 (2SD; Table 1; Fig. 3). The two duplicates (326.20–326.28 m) in the lower Velkerri Formation have $\varepsilon^{205}\text{Tl}_{\text{auth}}$ of -3.2 ± 0.4 and -3.6 ± 1.3, respectively, which are identical within analytical error.

Authigenic shale Tl concentrations of the Wollogorang Formation display no obvious distinctions between the upper (average Tl_{auth} of 0.90 ± 0.37 ppm, SE; ranging from 0.02 ppm to 2.05 ppm) and lower (average Tl_{auth} of 1.23 ± 0.24 ppm, SE; varying between 0.52 ppm and 1.56 ppm) intervals (Table 1; Fig. 4). There is essentially no difference between the authigenic Tl concentration of the dolomitized sample (1.35 ppm) and that of the shale sample with the same depth (1.49 ppm; Table 1; Fig. 4), given analytical uncertainties. The Tl isotopic compositions of the upper Wollogorang Formation (74.27–75.53 m) display a range between −5.9 to −3.9, with an average value of -4.7 ± 1.4 (Table 1; Fig. 4). The black shale samples from the lower Wollogorang Formation (76.00–76.96 m) have a similar average ε^{205}Tl value (-4.8 ± 0.4) but with a more restricted range (−5.1 to −4.6; Table 1; Fig. 4). The ε^{205}Tl value of the dolomitized sample from the lower Wollogorang Formation is -4.9 ± 1.3, which is indistinguishable from that of its duplicate (-4.6 ± 0.4) within analytical error (Table 1; Fig. 4). Neither of the formations are marked by significant stratigraphic variability in ε^{205}Tl values, except a minor difference in the average ε^{205}Tl values of the upper and lower Velkerri intervals.

6. DISCUSSION

6.1. Effects of post-depositional alteration on the Tl isotope composition of Wollogorang Formation black shales

The effect of post-depositional alteration on the Wollogorang shales can be evaluated by the degree of open-system behavior exhibited by the Re-Os isotope system (Kendall et al., 2009). Specifically, the extent of deviation from a reference ca. 1730 Ma Re-Os isochron (assuming a low seawater ^{187}Os/^{188}Os similar to most other Paleoproterozoic-Mesoproterozoic black shales) can be quantitatively assessed via calculating the percentage difference between the actual ^{187}Os/^{188}Os value and the ^{187}Os/^{188}Os value predicted by the reference isochron (Fig. 4). The Wollogorang black shales from the 76.00–76.96 m interval (lower Wollogorang) of the Mount Young 2 drill core have around one order magnitude larger

Table 1
Tl isotope composition and concentration of the authigenic fraction, Re-Os age, and percent deviation from the reference Re-Os isochron (only for Wollogorang samples) for the black shales of the Velkerri Formation and Wollogorang Formation.

Core depth[a] (m)	ε^{205}Tl	2SD	n	Tl (ppm)	Re-Os age[b] (Ma)	Deviation[c] (%)
Upper Velkerri (Urapunga-4)						
136.98–137.05	−2.0	0.3	3	8.67	1357	—
137.19–137.26	−3.1	0.0	2	8.22	1363	—
137.26–137.33	−2.2	0.1	2	6.64	1366	—
137.46–137.52	−2.6	0.2	2	9.15	1360	—
137.75–137.79	−2.1	0.5	6	8.23	1358	—
137.84–137.89	−2.5	0.5	2	7.51	1356	—
Lower Velkerri (Urapunga-4)						
325.71–325.78	−3.2	0.3	5	1.05	1419	—
326.20–326.28	−3.2	0.4	5	0.53	1411	—
326.20–326.28_dup	−3.6	1.3	6	0.51	—	—
326.42–326.48	−3.1	0.5	2	0.47	1408	—
326.48–326.55	−3.3	0.2	2	0.51	1420	—
326.62–326.69	−3.2	0.4	5	0.57	1417	—
Upper Wollogorang (Mount Young 2)						
74.27–74.29	−4.5	0.3	1	2.05	1724	−0.44
74.35–74.38	−3.9	0.3	4	0.20	1707	−1.42
75.08–75.11	−4.7	0.4	2	1.08	1726	−0.31
75.48–75.51	−5.9	0.5	2	0.02	1705	−1.56
75.51–75.53	−4.6	0.5	2	1.15	1725	−0.35
Lower Wollogorang (Mount Young 2)						
76.00–76.03	−5.1	0.3	1	0.52	1641	−5.25
76.03–76.08	−4.8	0.3	3	1.56	1613	−6.86
76.91–76.96	−4.6	0.4	4	1.49	1635	−5.61
76.91–76.96 (dol)	−4.9	1.3	7	1.35	1540	−11.10
76.91–76.96 (dol)_dup	−4.6	0.4	6	1.31	—	—

[a] "dup" represents duplicate full powder samples for Tl isotope analysis; "dol" denotes the black shale sample with dolomite veinlet.
[b] "Re-Os age" is calculated with assumed initial $^{187}Os/^{188}Os$ isotope ratio of 0.290 (at 1361 Ma) for upper Velkerri Formation, 0.060 (at 1417 Ma) for lower Velkerri Formation, and 0.115 (at 1730 Ma) for Wollogorang Formation. The age equation used is $(^{187}Os/^{188}Os)_{measured} = (^{187}Os/^{188}Os)_{initial} + (^{187}Re/^{188}Os)_{measured} \times (e^{\lambda t} - 1)$, where λ is the ^{187}Re decay constant of 1.666×10^{-11} a^{-1} (Smoliar et al., 1996; Selby et al., 2007) and t is derived Re-Os age for each sample. The $(^{187}Os/^{188}Os)_{measured}$ and $(^{187}Re/^{188}Os)_{measured}$ data for each sample are from Kendall et al. (2009) and presented in Table S2.
[c] "Deviation" denotes the percent deviation of sample points from the reference 1730 Ma Re-Os isochron. It is calculated by the percent difference between the actual $^{187}Os/^{188}Os$ value of the sample and the $^{187}Os/^{188}Os$ value predicted by the 1730 Ma Re-Os isochron given the $^{187}Re/^{188}Os$ value of the sample. The Re-Os isotope data are from Kendall et al. (2009) and presented in Table S2.

negative deviations from the reference 1730 Ma Re-Os isochron compared to the samples from the 74.27–75.53 m subset (upper Wollogorang; Fig. 4; Table 1; Kendall et al., 2009). Moreover, the sample with a prominent dolomite veinlet near the base of the lower Wollogorang interval (76.91–76.96 m) has the most pronounced negative deviation (Fig. 4; Table 1), suggesting that hydrothermal fluids percolated the black shale strata of the Wollogorang Formation from the underlying dolostone (Fig. 4; Donnelly and Jackson, 1988; Kendall et al., 2009) and migrated stratigraphically upward. The direction of deviation can be ascribed to artificially elevated $^{187}Re/^{188}Os$ ratios caused by preferential depletion of Os relative to Re or addition of Re relative to Os during hydrothermal fluid alteration (Kendall et al., 2009). The regression of Re-Os isotope data for Wollogorang shales yields Re-Os isochron dates of 1781 ± 190 Ma for the upper Wollogorang interval and 1234 ± 370 Ma for the lower Wollogorang interval, respectively (Kendall et al., 2009). The Re-Os isochron age of the upper Wollogorang shales (initial $^{187}Os/^{188}Os$ of −0.5 ± 1.9, 2SD; Kendall et al., 2009), though imprecise, is broadly consistent with independent U-Pb age constraints (1729 ± 4 Ma and 1730 ± 3 Ma), indicating that the upper Wollogorang interval was less perturbed by hydrothermal fluids. The lower Wollogorang interval shales (initial $^{187}Os/^{188}Os$ of 4.8 ± 4.3, 2SD; Kendall et al., 2009), however, was strongly altered by hydrothermal fluids as demonstrated by the unreasonably young Re-Os isochron date (Page et al., 2000; Kendall et al., 2009).

In an attempt to assess the effects of post-depositional hydrothermal alteration on Tl isotope records of the Wollogorang shales, we use the co-occurring Re-Os isotope systematics to gauge degrees of alteration, as was done previously for Mo and U isotopes (Kendall et al., 2009; Yang et al., 2017). The ε^{205}Tl of black shales from the upper Wollogorang interval (−4.7 ± 1.4) is indistinguishable within uncertainty from that of the deep Wollogorang subset (−4.8 ± 0.4; Fig. 4). No systematic correlation is

observed between ε^{205}Tl values and the percent deviation from the reference 1730 Ma Re-Os isochron (Fig. 4). In addition, there is no difference in Tl isotopic values between the dolomitic shale (most clearly altered based on petrography and Re-Os data) and the other samples (Fig. 4). The abundances of Tl display no variation trend between the upper (0.90 ± 0.37 ppm, SE) and lower (1.23 ± 0.24 ppm, SE) Wollgorang shales (Fig. 4; Table 1). Given the consistent Re-Os isochron age and U-Pb age of the upper Wollogorang interval, it is possible that the upper Wollogorang shales still record contemporaneous authigenic ε^{205}Tl signals. However, the trace metal systematics of lower Wollogorang shales are likely to have been disturbed in light of the strong evidence for open-system behavior in the Re-Os system.

The apparent independence between the Tl isotopic values and the extent of alteration (as evaluated by deviation from the reference 1730 Ma Re-Os isochron) can be explained by two possibilities: (1) the Tl isotope systematics of the Wollogorang shales have not been substantially altered during post-depositional hydrothermal alteration; or (2) the Tl isotope system has been homogeneously overprinted by post-depositional hydrothermal fluids in both the upper and lower Wollogorang intervals.

There are two possible scenarios (closed-system and open-system) that could in theory result in robust Tl isotope systematics in the face of post-depositional alteration of Wollogorang shales. In the first (closed-system alteration), the relatively oxidized mineralizing fluids did not effectively remobilize authigenic Tl from primary sulfide phases, which resulted in the retention of original Tl isotope signatures despite the disturbance to the Re-Os system. Alteration of Re-Os isotope systematics has been ascribed to the dissolution/reprecipitation of organic matter and sulfides (the major hosts for Re and Os). Since Tl in black shales appears to concentrate primarily in sulfides (Nielsen et al., 2009) while Re and Os in black shales are more prone to be hosted in organic matter rather than sulfides (Georgiev et al., 2012), one possible explanation for the distinct behaviors of Tl isotopes and Re-Os isotopes is that the hydrothermal fluids that altered Wollogorang shales only perturbed organic matter and did not significantly impact sulfide phases. In the second scenario (open system), Tl isotope fractionation during the leaching of Tl by hydrothermal fluids was limited. In other words, the relatively oxidizing alteration fluids may have leached Tl out of sulfide minerals at elevated temperature without imparting a significant isotope effect. If the removal of Tl was quantitative at the grain scale, the Tl isotopic compositions of the altered shales would exhibit minimal deviation from those of unaltered (or least altered) shales. This scenario finds some support in the observation that high-temperature, on-axis hydrothermal fluids are characterized by Tl isotopic compositions identical to those of average MORB, suggesting that the leaching of Tl from the oceanic crust does not lead to significant Tl isotope fractionation (Nielsen et al., 2006b). The postulated moderate to high temperature of the mineralization fluids (~100–200 °C) associated with alteration of the Wollogorang shales in Mount Young 2 may thus have caused limited Tl isotope fractionation during fluid alteration.

However, it is difficult to definitively rule out the possibility that post-depositional fluids have overprinted any authigenic Tl isotope signature initially preserved in the Wollogorang shales. The study of SEDEX metal index provides evidence of widespread Tl dispersion in the Wollogorang sediments (Spinks et al., 2016), suggesting the alteration fluids may have been enriched in Tl. If the abundance of authigenic Tl in Wollogorang shales was initially low and was followed by significant Tl capture from the fluid, any primary Tl isotope signature would have been overprinted. In this scenario, the ε^{205}Tl recorded in Wollogorang shales primarily reflects the Tl isotope composition of alteration fluids. The lack of difference in Tl isotopic values between the upper and lower Wollogorang shales implies that even the least altered upper Wollogorang interval has been completely overprinted by alteration fluids as a result of poor rock buffering relative to the Tl abundance of the alteration fluids, while the exogenous loading of Re and Os from the mineralizing fluids has not entirely masked the authigenic Re-Os isotope signature of the upper Wollogorang shales. Petrographic observations show that Tl-bearing diagenetic pyrite overgrowths are associated with sphalerite and galena mineralization, indicating the ore-bearing fluid that shaped the HYC Zn-Pb deposit had relatively high Tl abundances (Spinks et al., 2021). However, there is no obvious distinction in Tl concentration between the dolomitic shale (1.35 ppm) and the black shale of the same depth (1.49 ppm; Table 1; Fig. 4). In addition, Tl contents of the Wollgorang shales show no correlation with the percent deviation from the reference 1730 Ma Re-Os isochron (Fig. 4). These observations may suggest the alteration fluids that perturbed the Re-Os isotope systematics of the Wollogorang shales did not carry a significant amount of Tl. If Tl-bearing diagenetic pyrites precipitated during the local post-depositional alteration of the Wollogorang Formation (as in the case of HYC Pyritic Shale member; Spinks et al., 2021), Tl/S ratios might be helpful to gauge the amount of external Tl addition from the alteration fluids (i.e., the samples with larger extent of alteration are more likely to have low Tl/S ratios due to much smaller abundance of Tl in pyrite compared to S). However, we are unable to verify this assumption since whole-rock sulfur concentration data for the Wollogorang samples have not been determined.

We can also compare the behaviors of Tl, Mo, and U isotopes during post-depositional alteration of the Wollogorang shales. Both Mo and U isotope compositions vary systematically with the deviation from the 1730 Ma Re-Os reference isochron (Fig. 4), indicating that the extent of alteration had a significant effect on the δ^{98}Mo and δ^{238}U signatures of the lower Wollogorang shales. At face value, this pattern suggests that the upper Wollogorang interval may preserve authigenic Mo and U isotopic compositions, while the primary δ^{98}Mo and δ^{238}U values of the lower Wollogorang have been disturbed (similar to Re-Os isotope signatures). The altered lower Wollogorang shales have heavier U isotopic values and lighter Mo isotopic values compared to the more pristine upper Wollogo-

rang interval (Fig. 4). This observation could be interpreted to reflect preferential leaching of lighter ^{235}U and heavier Mo isotopes (including ^{98}Mo) during alteration or that the Wollogorang shales preferentially trapped heavier ^{238}U and lighter Mo isotopes (including ^{95}Mo) from the hydrothermal fluids (Kendall et al., 2009; Yang et al., 2017). In any case, the distinctive behaviors between Tl isotopes and Mo-U isotopes during the post-depositional alteration result in the absence of correlations between $\varepsilon^{205}Tl$ and $\delta^{98}Mo$ and between $\varepsilon^{205}Tl$ and $\delta^{238}U$ for the Wollogorang shales (Fig. 4).

6.2. Thallium isotope evidence for global ocean redox at 1.36 Ga

6.2.1. The stable Tl isotope composition of seawater during the early Mesoproterozoic

Black shales from the upper Velkerri interval (136.98–137.89 m) have DOP values ≥ 0.9 (Table S1; Fig. 3), suggesting that the Roper Superbasin was stably euxinic during deposition of this interval (Raiswell et al., 2018). In addition, both the high [Mo] (106–119 ppm; Table S1) and elevated Mo/TOC ratios (13–16 ppm/wt.%; Yang et al., 2017) of the upper Velkerri black shales suggest that the Roper Superbasin was not strongly restricted during the deposition of the upper Velkerri interval. Otherwise, the stagnant basins would have developed Mo-depleted bottom waters (due to a faster rate of Mo burial in sediments compared to the rate of Mo recharge via deep water renewal) and thus have low Mo/TOC ratios in euxinic sediments (Algeo and Lyons, 2006). The closed-system behavior of the Re-Os system in black shales also suggests that the Velkerri Formation had not been perturbed by any post-depositional alteration. Together with evidence for persistent euxinic conditions and lack of severe basin restriction, we can use the upper Velkerri black shales as a tracer of contemporaneous global seawater, yielding an oceanic $\varepsilon^{205}Tl$ of -2.4 ± 0.8 (ε) at ~1.36 Ga.

In contrast, the lower Velkerri shows evidence for both ferruginous deposition and possibly local restriction, in the form of intermediate DOP values (0.43–0.51), sporadically elevated Fe_T/Al ratios, detectable but very muted Mo enrichments of ~6–9 ppm, and low Mo/TOC ratios (though the latter could also be explained by a relative lack of H_2S). Intermediate DOP values and Fe_T/Al ratios indicate a modest enrichment of pyritic Fe in sediments and accordingly anoxic but sulfide-limited pyrite formation during deposition (Berner, 1970; Raiswell et al., 1988; Canfield et al., 1996; Raiswell and Canfield, 1996; Wijsman et al., 2001; Lyons et al., 2003; Raiswell and Anderson, 2005; Lyons and Severmann, 2006). The authigenic Tl enrichment in the lower Velkerri shales (0.62 ± 0.09 ppm, SE) is about an order of magnitude lower compared to that in the upper Velkerri shales (8.07 ± 0.36 ppm, SE; Table 1; Fig. 3), also supporting the distinctive redox state of the depositional environments (and/or degree of basinal connection to the open ocean) for the two Velkerri intervals. We thus conservatively interpret the $\varepsilon^{205}Tl$ values of the lower Velkerri as providing a lower bound on contemporaneous seawater (-3.3 ± 0.4) (ε) or a local basinal signature independent of the open ocean $\varepsilon^{205}Tl$ if the lower Velkerri was deposited in a relatively restricted basin (by analogy with the Black Sea; Owens et al., 2017).

6.2.2. Thallium isotope mass-balance modeling

6.2.2.1. Statistical modeling of marine Tl isotope mass balance. In our model, the Tl concentration and Tl isotope composition of global seawater are defined by:

$$\frac{dM^{Tl}}{dt} = F_{in} - F_{AOC} - F_{Ox} - F_{Eux} - F_{Red}, \tag{1}$$

$$\begin{aligned}\frac{dM^{Tl}\varepsilon^{205}Tl_{sw}}{dt} = {} & F_{in}\varepsilon^{205}Tl_{in} \\ & - F_{AOC}\left(\varepsilon^{205}Tl_{sw} + \Delta^{205}Tl_{AOC-sw}\right) \\ & - F_{Ox}\left(\varepsilon^{205}Tl_{sw} + \Delta^{205}Tl_{Ox-sw}\right) \\ & - F_{Eux}\left(\varepsilon^{205}Tl_{sw} + \Delta^{205}Tl_{Eux-sw}\right) \\ & - F_{Red}\left(\varepsilon^{205}Tl_{sw} + \Delta^{205}Tl_{Red-sw}\right).\end{aligned} \tag{2}$$

where M^{Tl} represents the mass of dissolved Tl in the ocean reservoir. The symbol $\varepsilon^{205}Tl_i$ denotes the Tl isotopic composition of the global seawater (*sw*), average marine inputs (*in*), and the four dominant oceanic outputs (*AOC*: altered oceanic crust; *Ox*: oxic sediments; *Eux*: euxinic sediments; *Red*: non-sulfidic reducing sediments), respectively. The symbol F_i represents the annual input or output flux of Tl (mol yr^{-1}). The magnitude of Tl isotope fractionation between a marine Tl sink and seawater is expressed as $\Delta^{205}Tl_{X\text{-}sw}$ (X represents *AOC* or *Ox* or *Eux* or *Red*). When Eq. (1) and (2) are both equal to 0, the marine Tl isotope budget reaches a steady state (e.g., modern ocean).

We formulate a redox-sensitive Tl sink flux (F_{Ox}, F_{Eux}, and F_{Red}) following the approach of Reinhard et al. (2013) and Stockey et al. (2020):

$$F_i = b_i A f_i \alpha_i \frac{[Tl]_{sw}}{[Tl]_{M.sw}}, \tag{3}$$

where b_i represents the globally averaged Tl burial rate of a given sink environment (oxic, euxinic, and reducing), A is the overall seafloor area (assumed to be the same as that of the modern oceans), f_i represents the areal fraction of global seafloor characteristic of that sink, α_i represents a scaling parameter used to modulate the burial rate relative to the seafloor area of the sink, $[Tl]_{sw}$ is the mean Tl concentration of modeled seawater and $[Tl]_{M.sw}$ is the Tl concentration of the modern seawater. The Tl uptake flux via the altered oceanic crust is defined as:

$$F_{AOC} = \Delta[Tl]_M \frac{[Tl]_{sw}}{[Tl]_{M.sw}} F_{LHF}, \tag{4}$$

where $\Delta[Tl]_M$ is the Tl concentration anomaly between the seawater and low-temperature hydrothermal fluid in modern oceans ($\Delta[Tl]_M = [Tl]_{M.sw} - [Tl]_{M.LHF}$; $[Tl]_{M.LHF}$ is the modern Tl concentration of low-T hydrothermal fluids), F_{LHF} is the low-T hydrothermal fluid flux. The seafloor area of each sink environment is defined as:

$$A_i = A f_i. \tag{5}$$

The parameterization of burial rate scaling coefficient (α_i) for the oxic, euxinic, and reducing sinks follows the

derivations used in Stockey et al. (2020). The accumulation rate of Tl in oxic sediments is assumed to be linearly scaled with the ambient seawater Tl reservoir and independent of organic carbon remineralization, and thus α_{Ox} is assumed to be constant:

$$\alpha_{Ox} = 1, \tag{6}$$

The attenuation factors of Tl burial rate for the anoxic (euxinic plus reducing) and euxinic sink environment (α_{Anox} and α_{Eux}) are implemented as a function of water depth which considers the effect of early diagenesis:

$$\alpha_{Anox} = \frac{\sum_{i=1}^{N_{Anox}} (1.58 - 0.16\ln(z_{Anox}))}{N_{Anox}}, \tag{7}$$

$$\alpha_{Eux} = \frac{\sum_{i=1}^{N_{Eux}} (1.58 - 0.16\ln(z_{Eux}))}{N_{Eux}}, \tag{8}$$

where z_i (i represents *Anox* or *Red*) is the modeled water depth of anoxic or euxinic environments, and N_i is the number of depth bins for the corresponding environment. In the above equation, z_i represents the maximum water depth of the anoxic or euxinic seafloor which is inverted from the modeled seafloor area (A_{Anox} or A_{Eux}) via a LOESS regression model to fit the bathymetric data (Menard and Smith, 1966). The numerator is the cumulative sum of organic matter flux with the expression derived from the remineralization model in Middelburg et al. (1996). The Tl burial rates scaling in the anoxic and euxinic sinks are thus implemented as a function of the cumulative average (tuning to the bathymetric depth of euxinic and reducing seafloor) of the organic carbon flux. The attenuation factor for the Tl burial rate in the reducing sink is formulated as the weighted subtraction between α_{Anox} and α_{Eux}.

$$\alpha_{Red} = \frac{|\alpha_{Anox} \times N_{Anox} - \alpha_{Eux} \times N_{Eux}|}{N_{Anox} - N_{Eux}}. \tag{9}$$

We employ a Monte Carlo approach to simulate marine Tl isotope mass balance, using the parameters given in Tables 2 and 3. The parameter ranges for Tl isotope fractionation factors ($\Delta^{205}Tl_{Ox\text{-}sw}$ and $\Delta^{205}Tl_{AOC\text{-}sw}$), the average Tl isotopic value of oceanic inputs ($\varepsilon^{205}Tl_{in}$), and the source fluxes are compiled from published observations. Removal fluxes are inverted from the modern flux estimates and modern estimated seafloor coverage of the associated sinks. A uniform (noninformative) prior distribution is assumed for all ten model variables (Table 3).

The goal of this Monte Carlo analysis is to generate the probability distribution of feasible seawater Tl isotope compositions associated with changes in the areal fractions of each redox-sensitive sink (f_{Ox}, f_{Anox}, and f_{Eux}). A logarithmically scaled step size is adopted in the simulations to generate 31 equally spaced bins for f_{Ox} (Fig. 5a and b), f_{Anox} (Fig. 5c and d), and f_{Eux} (Fig. 5e and f). For each f_{Ox} (or f_{Anox} or f_{Eux}) scenario, 1,000 model runs are performed with variable values randomly selected from the assumed prior distributions. The correlation among the areal fractions of redox sinks is defined as:

$$f_{Eux} = f_{Ds.max} - f_{Ox} - f_{Red}, \tag{10}$$

$$f_{Anox} = f_{Eux} + f_{Red}. \tag{11}$$

The parameter $f_{Ds.max}$ is the maximum seafloor fraction that is available for sediment deposition. The range of $f_{Ds.max}$ is set to vary between 90% (the total areal fraction of depositional seafloor in the modern ocean; Reinhard et al., 2013) and 100% (bounded by the physical oceanographic limit; Table 3). Note that a reducing Tl sink is implemented in the oceanic Tl isotope mass balance with the Tl burial rate range set as one tenth of that in the euxinic sink ($b_{Red.min} = 1/10\ b_{Eux.min}$ and $b_{Red.max} = 1/10\ b_{Eux.max}$; Table 3) and with a Tl isotope fractionation from seawater of 0 (Table 2). The framework of our model is meant primarily to compare the fractions of oxic, anoxic, and euxinic seafloor coverage at 1.4 Ga (derived from the marine Tl isotope mass balance) relative to those of the modern Earth.

The ordinary differential equations for Tl concentration and isotope mass balance [Eq. (1) and (2)] are solved with the Variable coefficient Ordinary Differential Equations (VODE) solver in the R package deSolve (Soetaert et al., 2010). The initial marine Tl concentration and Tl isotope composition of global seawater are set at the modern values (Table 2). The model is then run dynamically for 10 million years to ensure a steady-state simulation for each randomly sampled parameter set. The synthetic Tl isotopic values of euxinic black shales are then defined by the seawater isotopic value, based on the assumption of quantitative removal of Tl from local seawater during euxinic deposition (Owens et al., 2017). The Tl isotope mass balance model yields estimates for median f_{Ox} of 93.9% (95% credible interval of 89.2–98.8%), median f_{Anox} of 0.6% (95% credible interval of 0.1–3.9%), and median f_{Eux} of 0.2% (95% credible interval of 0.0–1.2%) with the modern seawater Tl isotope value ($\varepsilon^{205}Tl = -6.0 \pm 0.6$), which are all consistent with the areal fractions of modern oxic (84–94%), anoxic (0.1–2.0%), and euxinic (0.1–0.2%) seafloor, respectively (Fig. 5). The modeled sedimentary $\varepsilon^{205}Tl_{Eux}$ (identical to

Table 2
The constants of oceanographic and Tl isotope parameters for the Monte Carlo marine Tl isotope mass balance model.

Constant	Value	Unit	Reference
Modern global seafloor area, A	3.6×10^{14}	m^2	5
Modern marine Tl concentration, $[Tl]_{M.sw}$	65×10^{-12}	mol kg^{-1}	1
Tl isotope composition of modern seawater, $\varepsilon^{205}Tl_{sw}$	−6.0	ε	2, 4, 7
Tl isotope fractionation of euxinic sink, $\Delta^{205}Tl_{Eux\text{-}sw}$	0.0	ε	7
Tl isotope fractionation of reducing sink, $\Delta^{205}Tl_{Red\text{-}sw}$	0.0	ε	8, 9
Modern Tl concentration anomaly between seawater and low-T hydrothermal fluid, $\Delta[Tl]_M$	2.03×10^{-11}	mol kg^{-1}	3, 4, 6

References: 1: Flegal and Patterson, 1985; 2: Rehkämper et al., 2002; 3: Rehkämper and Nielsen, 2004; 4: Nielsen et al., 2006b; 5: Charette and Smith, 2010; 6: Nielsen et al., 2017; 7: Owens et al., 2017; 8: Fan et al., 2020; 9: Ostrander et al., 2020.

Table 3
The minimum and maximum values of parameters for the Monte Carlo marine Tl isotope mass balance model.

Variable	Minimum value	Maximum value	Unit	Reference
Tl isotope fractionation of oxic sink, $\Delta^{205}Tl_{Ox\text{-}sw}$	13.5	19.0	ε	1, 2, 7, 9, 13
Tl isotope fractionation of alteration of oceanic crust, $\Delta^{205}Tl_{AOC\text{-}sw}$	−2.5	0.0	ε	5, 10, 12, 13
Flux of oceanic Tl input, F_{in}	3.87×10^{6}	6.05×10^{6}	mol yr^{-1}	3, 13
Flux of low temperature hydrothermal fluid, F_{LHF}	1.20×10^{17}	1.88×10^{17}	kg yr^{-1}	3, 5, 13
Tl burial rate in oxic sediments, b_{Ox}	4.10×10^{-9} [a]	6.41×10^{-9} [a]	mol m^{-2} yr^{-1}	11, 13
Tl burial rate in euxinic sediments, b_{Eux}	3.93×10^{-7} [a]	6.14×10^{-7} [a]	mol m^{-2} yr^{-1}	8, 11, 14
Tl burial rate in reducing sediments, b_{Red}	3.93×10^{-8} [b]	6.14×10^{-8} [b]	mol m^{-2} yr^{-1}	—
Tl isotope composition of oceanic Tl input, $\varepsilon^{205}Tl_{in}$	−2.5	−1.0	ε	4, 5, 6, 13
Maximum areal fraction of depositional seafloor, $f_{Ds.max}$	90	100	%	11
Areal fraction of euxinic seafloor, f_{Eux}	0	f_{Anox}	%	—

References: 1: Rehkämper et al., 2002; 2: Rehkämper et al., 2004; 3: Rehkämper and Nielsen, 2004; 4: Nielsen et al., 2005; 5: Nielsen et al., 2006b; 6: Baker et al., 2009; 7: Nielsen et al., 2009; 8: Nielsen et al., 2011; 9: Nielsen et al., 2013; 10: Prytulak et al., 2013; 11: Reinhard et al., 2013; 12: Coggon et al., 2014; 13: Nielsen et al., 2017; 14: Owens et al., 2017.

[a] The Tl burial rates of redox-sensitive sinks (oxic and euxinic) are calculated from the output flux range and the seafloor area associated with that sink environment in the modern ocean.

[b] The range of Tl burial rate (both the min and max value) in reducing sink is scaled as one tenth of the burial rate in euxinic sink.

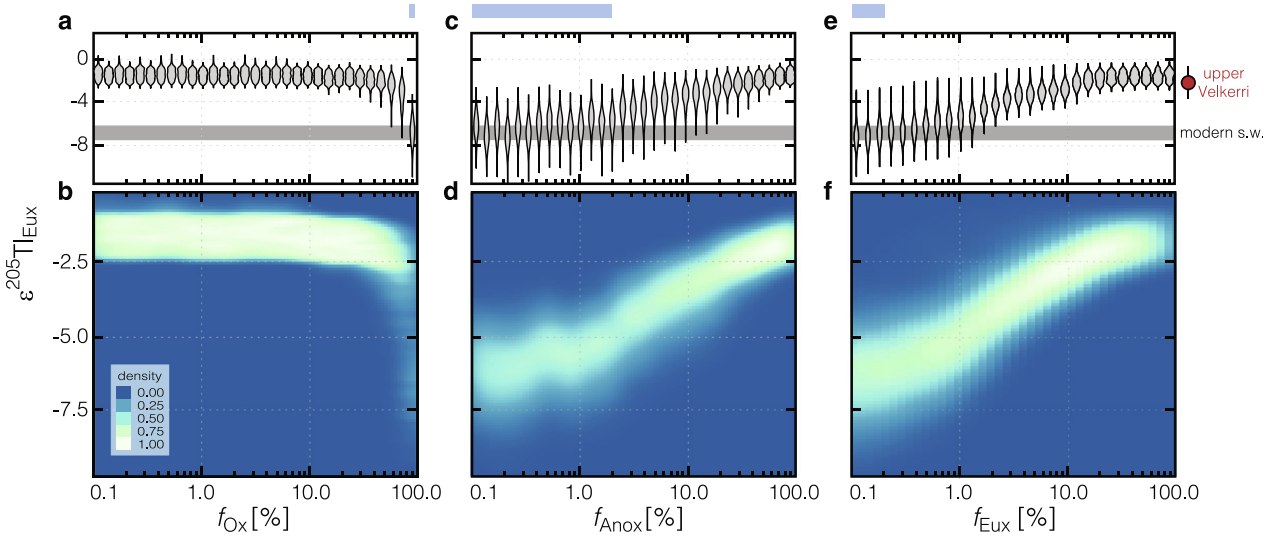

Fig. 5. Violin plots and two-dimensional heat maps illustrating the frequency distribution of modeled Tl isotope compositions of euxinic sediments ($\varepsilon^{205}Tl_{Eux}$) as a function of logarithmically scaled oxic (f_{Ox}; a and b), anoxic (f_{Anox}; c and d), and euxinic (f_{Eux}; e and f) seafloor areal fraction in our statistical isotope mass balance model. The f_{Anox} is calculated as the sum of euxinic (f_{Eux}) and reducing (f_{Red}) seafloor areal fraction. The $\varepsilon^{205}Tl_{Eux}$ is calculated via the Monte Carlo analysis of marine Tl isotope mass balance. The $\varepsilon^{205}Tl_{Eux}$ of the upper Velkerri interval is labeled at the right-side panel with the red circle denoting the median value and error bars representing the data range. The dark grey bars across the violin plots denote the $\varepsilon^{205}Tl$ of the modern seawater. The blue shaded rectangles on top of violin plots represent the areal fractions of modern oxic, anoxic, and euxinic seafloor (f_{Ox}: 84–94%; f_{Anox}: 0.1–2.0%; f_{Eux}: 0.1–0.2%), respectively.

$\varepsilon^{205}Tl_{sw}$) generally shifts to isotopically lighter values with expanding f_{Anox} and f_{Eux}. The spatial extent of euxinic seafloor (f_{Eux}) exerts first-order control on the correlation between $\varepsilon^{205}Tl_{Eux}$ and f_{Anox} with the impact of a reducing sink for Tl increasing the statistical spread of feasible $\varepsilon^{205}Tl_{Eux}$ values (Fig. 5c-f).

6.2.2.2. Global ocean redox at 1.36 Ga: Implications from a statistical model of marine Tl isotope mass balance. Our statistical model of Tl isotope mass balance yields a frequency distribution of steady-state values for $\varepsilon^{205}Tl_{Eux}$ given a prescribed seafloor redox landscape (f_{Ox} or f_{Anox} or f_{Eux}). The Tl isotope values of 1.36 Ga seawater (−2.4 ± 0.8) constrained from upper Velkerri euxinic shale records are within the $\varepsilon^{205}Tl$ range of oceanic inputs (from −2.5 to −1.0). As a result, the areal fraction of oxic seafloor at 1.36 Ga implied by the Tl isotope mass balance model is difficult to delineate precisely because seawater Tl isotope values are largely invariant across orders of magnitude in f_{Ox} (Fig. 5a). Indeed, the Tl isotope proxy becomes sensitive to the proportion of oxic seafloor only when f_{Ox} is higher than ~30% due to existing analytical precision. In any case, our results do indicate f_{Ox} values at 1.36 Ga (median value of 5.0% and 95th percentile of 63.1%) well below those of

the modern Earth (Fig. 5a and b), suggesting that the burial of Mn-oxides in marine sediments was limited on a global scale at 1.36 Ga. The model results also suggest median f_{Anox} of 31.6% (5th percentile of 6.3%) and median f_{Eux} of 4.3% (5th percentile of 2.0%) at 1.36 Ga (Fig. 5c-f), representing a significant expansion of anoxic and euxinic deposition relative to that of the modern oceans (0.1–2.0% anoxic and 0.1–0.2% euxinic seafloor areas), which is consistent with inferences of a pervasively anoxic ocean interior. This result is generally aligned with elemental oceanic mass balance models that estimated the extent of seafloor anoxia to be ~13% at 1.36 Ga using Re (Sheen et al., 2018), and ~30–40% during the mid-Proterozoic using Cr (Reinhard et al., 2013). The expansion of marine euxinia is supported by the conclusion that roughly ~2% of the seafloor was overlain by strongly euxinic conditions at 1.36 Ga (derived from Mo and U isotope data of the upper Velkerri Formation and coupled Mo-U isotope mass balance modeling; Kendall et al., 2009; Yang et al., 2017; Lu et al., 2020) and no more than 7% global seafloor euxinia during the mid-Proterozoic (from U isotope and Mo elemental mass balance models; Reinhard et al., 2013; Gilleaudeau et al., 2019). In addition, the prominent decrease in the extent of oxic seafloor at 1.36 Ga relative to today is broadly consistent with unfractionated $\delta^{53}Cr$ signatures of the upper Velkerri Formation (inactive oxidative Cr cycling implies sufficiently low atmospheric O_2 levels; Cole et al., 2016).

Our results cannot rule out the suggestion of transient ocean oxygenation at ~1.4 Ga, as suggested by some recent work (Cox et al., 2016; Zhang et al., 2016, 2019; Hardisty et al., 2017; Yang et al., 2017; Canfield et al., 2018; Diamond and Lyons, 2018; Diamond et al., 2018; Sheen et al., 2018; Mukherjee et al., 2019; Liu et al., 2020; Lu et al., 2020; Wang et al., 2020). In particular, it is possible that mild oxygenation of some regions of the ocean interior occurred at levels that were not sufficiently well-oxygenated to support robust Mn-oxide precipitation and long-term burial in marine sediments but were capable of being registered in other isotopic and trace element proxies. We also note that an expansion of euxinic environments during the deposition of the upper Velkerri interval may be in line with a pulse of ocean oxygenation at ~1.36 Ga. In particular, the enhancement of benthic euxinia indicates accelerated rates of sulfide production via sulfate reduction, possibly linked to increasing concentrations of oceanic sulfate (suggested by the sulfur isotope data of the upper Velkerri Formation; Shen et al., 2003) and potential deep ocean oxygenation (to sustain the expanded marine sulfate reservoir via the oxidation of reduced sulfur with molecular oxygen). Nevertheless, our results strongly suggest that any such transient oxygenation of the ocean interior (below the mixed layer and beyond the shelf-slope break) was significantly different in scale and intensity from that of the modern Earth, and that the anoxic waters covered a

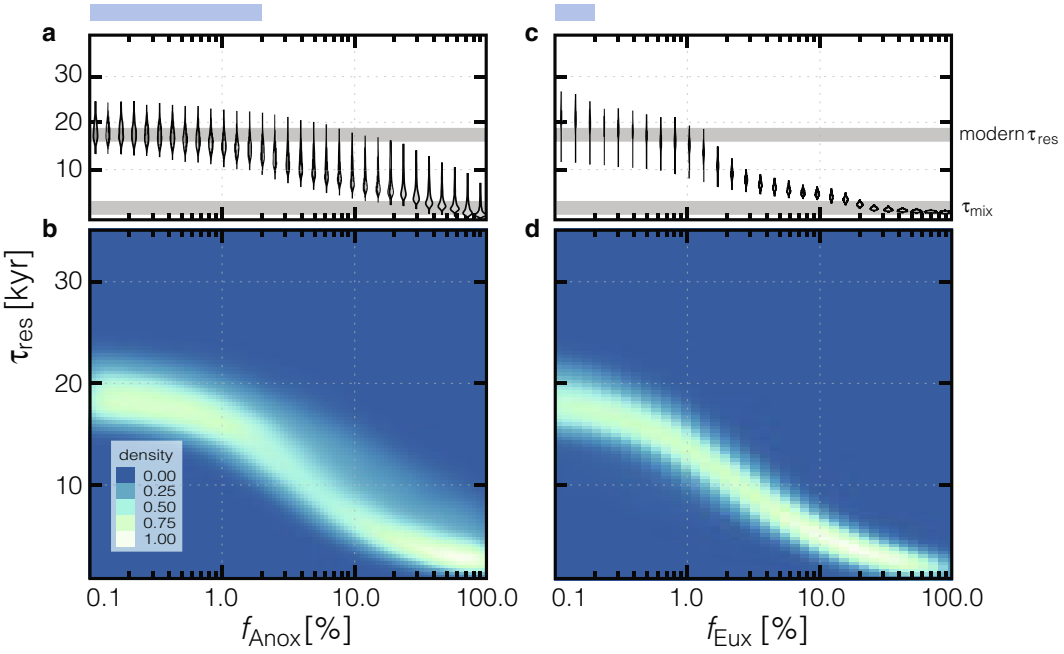

Fig. 6. Violin plot and two-dimensional heat map of modeled marine Tl residence time (τ_{res}) as a function of logarithmically scaled anoxic (f_{Anox}; a and b) or euxinic (f_{Eux}; c and d) seafloor areal fraction in our statistical isotope mass balance model. The f_{Anox} is calculated as the sum of euxinic (f_{Eux}) and reducing (f_{Red}) seafloor areal fraction. The τ_{res} is calculated from the modeled marine Tl concentration and the corresponding oceanic Tl fluxes of each Monte Carlo run. The frequency distribution of τ_{res} for the 31 f_{Anox} or f_{Eux} bins is shown as the probability density in the heat map and kernel density estimation in the violin plot. The dark grey and light grey bars in the violin plot denote modern Tl residence time (~18.5 kyrs) and ocean mixing time (~1000 years), respectively. The blue shaded rectangles on top of violin plots represent the areal fractions of modern anoxic (f_{Anox}: 0.1–2.0%) and euxinic seafloor (f_{Eux}: 0.1–0.2%), respectively.

majority of the ocean floor during deposition of the upper Velkerri Formation.

The Monte Carlo analysis of Tl isotope mass balance modeling can also provide insight into the oceanic residence time of Tl (τ_{res}). Significantly, the Tl residence time declines with the increasing extent of anoxic seafloor (Fig. 6a and b), which is dominated by the expansion of euxinia (Fig. 6c and d) driven by the increased sink strength for Tl in sulfidic depositional settings. As τ_{res} approaches the ocean mixing timescale (~1000 years) which occurs when the areal extent of euxinic seafloor (f_{Eux}) exceeds ~20% (f_{Anox} approaching ~40%), this relationship will have an increasingly important impact on the interpretations of euxinic sediments as an archive for Tl isotopic values of contemporaneous seawater. Specifically, the Tl isotope composition of seawater may become heterogeneous on a global scale when the marine Tl residence time is shorter than timescales of large-scale ocean mixing. The decrease in marine Tl residence time will also render Tl more sensitive to the effects of restriction—in that the ε^{205}Tl of local basinal water can more easily be decoupled from that of the open ocean when Tl inventories are small and residence times short. However, we find that this occurs only at levels of very intense euxinia where $f_{Eux} > 20\%$. Given that our statistical model suggests a f_{Eux} estimate of ~4% for the upper Velkerri ε^{205}Tl data, consistent with no more than 10% global seafloor euxinia during the mid-Proterozoic (Gilleaudeau et al., 2019; Reinhard et al., 2013), and that we see negligible stratigraphic variation in Tl isotope values, we consider it reasonable to assume that seawater Tl was isotopically homogenous during the deposition of the upper Velkerri black shales. The distinct probability distributions of f_{Ox}, f_{Anox}, and f_{Eux} at 1.36 Ga compared to those of the modern oceans thus strongly imply that the global burial of Mn-oxides was very limited at 1.36 Ga.

7. CONCLUSIONS

The average $\varepsilon^{205}Tl_{auth}$ of the upper Velkerri Formation, together with the overall paleoredox geochemistry and a precise Re-Os isochron yielding an age consistent with independent depositional age constraints, suggests that the Tl isotope composition of global seawater at 1.36 Ga was -2.4 ± 0.8 (ε). We interpret the Tl isotope value recorded by the lower Velkerri interval (-3.3 ± 0.4) as providing a lower bound on contemporaneous seawater due to a non-euxinic (ferruginous) or highly restricted depositional environment. Although our Tl isotope mass balance model suggests that the seafloor redox landscape is a major control on the marine Tl inventory, only very extensive euxinia is likely to result in a heterogeneous marine Tl isotope distribution. We thus consider it likely that the upper Velkerri sediments record a homogeneous contemporaneous global seawater Tl isotope signal given independent evidence against severe basin restriction from the open ocean, such as elevated Mo concentrations and Mo/TOC ratios. A statistical analysis of a Tl isotope mass-balance model suggests that the global burial of Mn-oxides was limited at 1.36 Ga, which indicates that the contemporaneous deep ocean was primarily anoxic during deposition of the upper Velkerri Formation. Although the Tl isotope data do not preclude the possibility of a transient ocean oxygenation event at around 1.4 Ga, this study adds to a growing body of evidence that the mid-Proterozoic Earth system was fundamentally distinct from that of the modern Earth.

Stable Tl isotope data from black shales of the Paleoproterozoic Wollogorang Formation remain invariant despite greater deviations of Re-Os isotope data from a reference 1730 Ma Re-Os isochron towards the base of the Wollogorang black shale unit, in contrast to the behavior observed for the Mo and U isotope systems. Although there is no systematic relationship between ε^{205}Tl values and the extent of alteration as estimated by open-system Re-Os behavior, it is difficult to definitively rule out the possibility that authigenic Tl isotope signatures have been overprinted by later hydrothermal fluid alteration. We consider it questionable to leverage these data to infer the global ocean redox conditions at 1.73 Ga considering the disturbed isotope systematics of Re-Os, Mo, and U, at least at this locality. These observations highlight the insights provided by evaluating open-system behavior via combined application of radiogenic isotope systems together with other stable isotope tracers for reconstructing the redox landscape of Earth's oceans over time.

Declaration of Competing Interest

The authors declare that they have no known competing financial interests or personal relationships that could have appeared to influence the work reported in this paper.

ACKNOWLEDGEMENTS

We would like to thank Brett Holdaway, Theodore Them, and Fei Wu for assistance in the lab. This research was supported by the NASA Interdisciplinary Consortia for Astrobiology Research (C.T.R.) and NASA Astrobiology Early Career Collaboration Award (Z.L.). Constructive comments from Marcus Kunzmann, Svet Georgiev, and one anonymous reviewer, and careful handling by the Associate Editor Susan Little are greatly appreciated. Support from the Canada Research Chairs Program and a NSERC Discovery Grant (RGPIN-2019-04090) is gratefully acknowledged (B.K.). Support for analysis from NASA Exobiology NNX16AJ60 and 80NSSC18K1532 (J.D.O.) and by the National High Magnetic Field Laboratory (Tallahassee, Florida), which is funded by the National Science Foundation Cooperative Agreement No. DMR1644779 and the State of Florida.

APPENDIX A. SUPPLEMENTARY MATERIAL

Supplementary data to this article can be found online at https://doi.org/10.1016/j.gca.2021.09.006.

REFERENCES

Abbott S. T. and Sweet I. P. (2000) Tectonic control on third-order sequences in a siliciclastic ramp-style basin: an example from the Roper Superbasin (Mesoproterozoic), northern Australia. *Austrian J. Earth Sci.* **47**, 637–657.

Ahmad, M. and Dunster, J. (2013) Chapter 15: McArthur Basin: in Ahmad M and Munson TJ (compilers)'. Geology and mineral

resource of the Northern Territory'. Northern Territory Geological Survey, Special Publication 5.

Algeo T. J. and Lyons T. W. (2006) Mo-total organic carbon covariation in modern anoxic marine environments: Implications for analysis of paleoredox and paleohydrographic conditions. *Paleoceanography* **21**, PA1016.

Arnold G. L., Anbar A. D., Barling J. and Lyons T. W. (2004) Molybdenum isotope evidence for widespread anoxia in mid-Proterozoic oceans. *Science* **304**, 87–90.

Baker R. G. A., Rehkämper M., Hinkley T. K., Nielsen S. G. and Toutain J. P. (2009) Investigation of thallium fluxes from subaerial volcanism—Implications for the present and past mass balance of thallium in the oceans. *Geochim. Cosmochim. Acta* **73**, 6340–6359.

Bellefroid E. J., Hood A. V. S., Hoffman P. F., Thomas M. D., Reinhard C. T. and Planavsky N. J. (2018) Constraints on Paleoproterozoic atmospheric oxygen levels. *Proc. Natl. Acad. Sci. U. S. A.* **115**, 8104–8109.

Berner R. A. (1970) Sedimentary pyrite formation. *Am. J. Sci.* **268**, 1–23.

Bidoglio G., Gibson P., O'Gorman M. and Roberts K. (1993) X-ray absorption spectroscopy investigation of surface redox transformations of thallium and chromium on colloidal mineral oxides. *Geochim. Cosmochim. Acta* **57**, 2389–2394.

Bodorkos S., Crowley J., Claoué-Long J., Anderson J. and Magee, , C. (2021) Precise U-Pb baddeleyite dating of the Derim Derim Dolerite, McArthur Basin, Northern Territory: old and new SHRIMP and ID-TIMS constraints. *Austrian J. Earth Sci.* **68**, 36–50.

Bowman C. N., Young S. A., Kaljo D., Eriksson M. E., Them T. R., Hints O., Martma T. and Owens J. D. (2019) Linking the progressive expansion of reducing conditions to a stepwise mass extinction event in the late Silurian oceans. *Geology* **47**, 968–972.

Boyle R. A., Clark J. R., Poulton S. W., Shields-Zhou G., Canfield D. E. and Lenton T. M. (2013) Nitrogen cycle feedbacks as a control on euxinia in the mid-Proterozoic ocean. *Nat. Commun.* **4**, 1533.

Canfield D. E., Lyons T. W. and Raiswell R. (1996) A model for iron deposition to euxinic Black Sea sediments. *Am. J. Sci.* **296**, 818–834.

Canfield D. E., Zhang S., Frank A. B., Wang X., Wang H., Su J., Ye Y. and Frei R. (2018) Highly fractionated chromium isotopes in Mesoproterozoic-aged shales and atmospheric oxygen. *Nat. Commun.* **9**, 2871.

Charette M. A. and Smith W. H. (2010) The volume of Earth's ocean. *Oceanography* **23**, 112–114.

Chen K., Walker R. J., Rudnick R. L., Gao S., Gaschnig R. M., Puchtel I. S., Tang M. and Hu Z.-C. (2016) Platinum-group element abundances and Re–Os isotopic systematics of the upper continental crust through time: Evidence from glacial diamictites. *Geochim. Cosmochim. Acta* **191**, 1–16.

Coggon R. M., Rehkämper M., Atteck C., Teagle D. A. H., Alt J. C. and Cooper M. J. (2014) Controls on thallium uptake during hydrothermal alteration of the upper ocean crust. *Geochim. Cosmochim. Acta* **144**, 25–42.

Cole D. B., Planavsky N. J., Longley M., Böning P., Wilkes D., Wang X., Swanner E. D., Wittkop C., Loydell D. K., Busigny V., Knudsen A. C. and Sperling E. A. (2020) Uranium isotope fractionation in non-sulfidic anoxic settings and the global uranium isotope mass balance. *Global Biogeochem. Cy.* **34**, e2020GB006649.

Cole D. B., Reinhard C. T., Wang X., Gueguen B., Halverson G. P., Gibson T., Hodgskiss M. S. W., McKenzie N. R., Lyons T. W. and Planavsky N. J. (2016) A shale-hosted Cr isotope record of low atmospheric oxygen during the Proterozoic. *Geology* **44**, 555–558.

Cooke D. R., Bull S. W., Donovan S. and Rogers J. R. (1998) K-metasomatism and base metal depletion in volcanic rocks from the McArthur Basin, Northern Territory; implications for base metal mineralization. *Econ. Geol.* **93**, 1237–1263.

Cooke D. R., Bull S. W., Large R. R. and McGoldrick P. J. (2000) The importance of oxidized brines for the formation of Australian Proterozoic stratiform sediment-hosted Pb-Zn (Sedex) deposits. *Econ. Geol.* **95**, 1–18.

Cox G. M., Jarrett A., Edwards D., Crockford P. W., Halverson G. P., Collins A. S., Poirier A. and Li Z.-X. (2016) Basin redox and primary productivity within the Mesoproterozoic Roper Seaway. *Chem. Geol.* **440**, 101–114.

Creaser R. A., Sannigrahi P., Chacko T. and Selby D. (2002) Further evaluation of the Re-Os geochronometer in organic-rich sedimentary rocks: A test of hydrocarbon maturation effects in the Exshaw Formation, Western Canada Sedimentary Basin. *Geochim. Cosmochim. Acta* **66**, 3441–3452.

Crick I. H., Boreham C. J., Cook A. C. and Powell T. G. (1988) Petroleum Geology and Geochemistry of Middle Proterozoic McArthur Basin, Northern Australia II: Assessment of Source Rock Potential1. *AAPG Bull.* **72**, 1495–1514.

Daines S. J., Mills B. J. and Lenton T. M. (2017) Atmospheric oxygen regulation at low Proterozoic levels by incomplete oxidative weathering of sedimentary organic carbon. *Nat. Commun.* **8**, 14379.

Derry L. A. (2015) Causes and consequences of mid-Proterozoic anoxia. *Geophys. Res. Lett.* **42**, 8538–8546.

Dhuime B., Hawkesworth C. J., Delavault H. and Cawood P. A. (2018) Rates of generation and destruction of the continental crust: implications for continental growth. *Philos. Trans. A. Math. Phys. Eng. Sci.* **376**, 20170403.

Dhuime B., Wuestefeld A. and Hawkesworth C. J. (2015) Emergence of modern continental crust about 3 billion years ago. *Nat. Geosci.* **8**, 552–555.

Diamond C. W. and Lyons T. W. (2018) Mid-Proterozoic redox evolution and the possibility of transient oxygenation events. *Emerg. Top. Life. Sci.* **2**, 235–245.

Diamond C. W., Planavsky N. J., Wang C. and Lyons T. W. (2018) What the ~1.4 Ga Xiamaling Formation can and cannot tell us about the mid-Proterozoic ocean. *Geobiology* **16**, 219–236.

Donnelly T. H. and Jackson M. J. (1988) Sedimentology and geochemistry of a mid-Proterozoic lacustrine unit from northern Australia. *Sediment. Geol.* **58**, 145–169.

Esser B. K. and Turekian K. K. (1993) The osmium isotopic composition of the continental crust. *Geochim. Cosmochim. Acta* **57**, 3093–3104.

Fan H., Nielsen S. G., Owens J. D., Auro M., Shu Y., Hardisty D. S., Horner T. J., Bowman C. N., Young S. A. and Wen H. (2020) Constraining oceanic oxygenation during the Shuram excursion in South China using thallium isotopes. *Geobiology* **18**, 348–365.

Flegal A. R. and Patterson C. C. (1985) Thallium concentrations in seawater. *Mar. Chem.* **15**, 327–331.

Garven G., Bull S. and Large R. (2001) Hydrothermal fluid flow models of stratiform ore genesis in the McArthur Basin, Northern Territory, Australia. *Geofluids* **1**, 289–311.

Georgiev S., Stein H. J., Hannah J. L., Weiss H. M., Bingen B., Xu G., Rein E., Hatlø V., Løseth H. and Nali M. (2012) Chemical signals for oxidative weathering predict Re–Os isochroneity in black shales, East Greenland. *Chem. Geol.* **324**, 108–121.

Gilleaudeau G. J., Frei R., Kaufman A. J., Kah L. C., Azmy K., Bartley J. K., Chernyavskiy P. and Knoll A. H. (2016) Oxygenation of the mid-Proterozoic atmosphere: clues from

chromium isotopes in carbonates. *Geochem. Perspect. Lett.* **2**, 178–187.

Gilleaudeau G. J. and Kah L. C. (2015) Heterogeneous redox conditions and a shallow chemocline in the Mesoproterozoic ocean: Evidence from carbon–sulfur–iron relationships. *Precambrian Res.* **257**, 94–108.

Gilleaudeau G. J., Romaniello S. J., Luo G., Kaufman A. J., Zhang F., Klaebe R. M., Kah L. C., Azmy K., Bartley J. K., Zheng W., Knoll A. H. and Anbar A. D. (2019) Uranium isotope evidence for limited euxinia in mid-Proterozoic oceans. *Earth Planet Sci. Lett.* **521**, 150–157.

Gilleaudeau G. J., Sahoo S. K., Ostrander C. M., Owens J. D., Poulton S. W., Lyons T. W. and Anbar A. D. (2020) Molybdenum isotope and trace metal signals in an iron-rich Mesoproterozoic ocean: A snapshot from the Vindhyan Basin, India. *Precambrian Res.* **343**, 105718.

Guilbaud R., Poulton S. W., Thompson J., Husband K. F., Zhu M., Zhou Y., Shields G. A. and Lenton T. M. (2020) Phosphorus-limited conditions in the early Neoproterozoic ocean maintained low levels of atmospheric oxygen. *Nat. Geosci.* **13**, 296–301.

Hardisty D. S., Lu Z., Bekker A., Diamond C. W., Gill B. C., Jiang G., Kah L. C., Knoll A. H., Loyd S. J., Osburn M. R., Planavsky N. J., Wang C., Zhou X. and Lyons T. W. (2017) Perspectives on Proterozoic surface ocean redox from iodine contents in ancient and recent carbonate. *Earth and Planetary Science Letters* **463**, 159–170.

Hattori Y., Suzuki K., Honda M. and Shimizu H. (2003) Re-Os isotope systematics of the Taklimakan Desert sands, moraines and river sediments around the Taklimakan Desert, and of Tibetan soils. *Geochim. Cosmochim. Acta* **67**, 1203–1213.

Hawkesworth C., Cawood P. and Dhuime B. (2013) Continental growth and the crustal record. *Tectonophysics* **609**, 651–660.

Helz G. R. and Dolor M. K. (2012) What regulates rhenium deposition in euxinic basins? *Chem. Geol.* **304**, 131–141.

Idnurm M. (2000) Towards a high resolution Late Palaeoproterozoic – earliest Mesoproterozoic apparent polar wander path for northern Australia. *Austrian J. Earth Sci.* **47**, 405–429.

Idnurm M., Giddings J. W. and Plumb K. A. (1995) Apparent polar wander and reversal stratigraphy of the Palaeo-Mesoproterozoic southeastern McArthur Basin, Australia. *Precambrian Res.* **72**, 1–41.

Jackson M. and Raiswell R. (1991) Sedimentology and carbon-sulphur geochemistry of the Velkerri Formation, a mid-Proterozoic potential oil source in northern Australia. *Precambrian Res.* **54**, 81–108.

Jackson M. J. (1985) Mid-proterozoic dolomitic varves and microcycles from the McArthur basin, Northern Australia. *Sediment. Geol.* **44**, 301–326.

Jackson M. J., Scott D. L. and Rawlings D. J. (2000) Stratigraphic framework for the Leichhardt and Calvert Superbasins: Review and correlations of the pre- 1700 Ma successions between Mt Isa and McArthur River. *Austrian J. Earth Sci.* **47**, 381–403.

Jaffe L. A., Peucker-Ehrenbrink B. and Petsch S. T. (2002) Mobility of rhenium, platinum group elements and organic carbon during black shale weathering. *Earth Planet Sci. Lett.* **198**, 339–353.

Johnston D. T., Farquhar J., Summons R. E., Shen Y., Kaufman A. J., Masterson A. L. and Canfield D. E. (2008) Sulfur isotope biogeochemistry of the Proterozoic McArthur Basin. *Geochim. Cosmochim. Acta* **72**, 4278–4290.

Kendall B., Creaser R. A., Gordon G. W. and Anbar A. D. (2009) Re–Os and Mo isotope systematics of black shales from the Middle Proterozoic Velkerri and Wollogorang Formations, McArthur Basin, northern Australia. *Geochim. Cosmochim. Acta* **73**, 2534–2558.

Kendall B. S., Creaser R. A., Ross G. M. and Selby D. (2004) Constraints on the timing of Marinoan "Snowball Earth" glaciation by ^{187}Re–^{187}Os dating of a Neoproterozoic, post-glacial black shale in Western Canada. *Earth Planet Sci. Lett.* **222**, 729–740.

Krissansen-Totton J. and Catling D. C. (2020) A coupled carbon-silicon cycle model over Earth history: Reverse weathering as a possible explanation of a warm mid-Proterozoic climate. *Earth Planet Sci. Lett.* **537**, 116181.

Kunzmann M., Crombez V., Catuneanu O., Blaikie T. N., Barth G. and Collins A. S. (2020) Sequence stratigraphy of the ca. 1730 Ma Wollogorang Formation, McArthur Basin, Australia. *Mar. Petrol. Geol.* **116** 104297.

Laakso T. A. and Schrag D. P. (2014) Regulation of atmospheric oxygen during the Proterozoic. *Earth Planet Sci. Lett.* **388**, 81–91.

Little S. H., Vance D., Walker-Brown C. and Landing W. M. (2014) The oceanic mass balance of copper and zinc isotopes, investigated by analysis of their inputs, and outputs to ferromanganese oxide sediments. *Geochim. Cosmochim. Acta* **125**, 673–693.

Liu A., Tang D., Shi X., Zhou X., Zhou L., Shang M., Li Y. and Fang H. (2020) Mesoproterozoic oxygenated deep seawater recorded by early diagenetic carbonate concretions from the Member IV of the Xiamaling Formation, North China. *Precambrian Res.* **341**.

Liu X. M., Kah L. C., Knoll A. H., Cui H., Kaufman A. J., Shahar A. and Hazen R. M. (2016) Tracing Earth's O_2 evolution using Zn/Fe ratios in marine carbonates. *Geochem. Perspect. Lett.* **2**, 24–34.

Logan G. A., Hinman M. C., Walter M. R. and Summons R. E. (2001) Biogeochemistry of the 1640 Ma McArthur River (HYC) lead-zinc ore and host sediments, Northern Territory, Australia. *Geochim. Cosmochim. Acta* **65**, 2317–2336.

Lowell R. P. and Keller S. M. (2003) High-temperature seafloor hydrothermal circulation over geologic time and archean banded iron formations. *Geophys. Res. Lett.* **30**, 1391.

Lu X., Dahl T. W., Zheng W., Wang S. and Kendall B. (2020) Estimating ancient seawater isotope compositions and global ocean redox conditions by coupling the molybdenum and uranium isotope systems of euxinic organic-rich mudrocks. *Geochim. Cosmochim. Acta* **290**, 76–103.

Lyons T. W., Reinhard C. T. and Planavsky N. J. (2014) The rise of oxygen in Earth's early ocean and atmosphere. *Nature* **506**, 307–315.

Lyons T. W. and Severmann S. (2006) A critical look at iron paleoredox proxies: New insights from modern euxinic marine basins. *Geochim. Cosmochim. Acta* **70**, 5698–5722.

Lyons T. W., Werne J. P., Hollander D. J. and Murray R. W. (2003) Contrasting sulfur geochemistry and Fe/Al and Mo/Al ratios across the last oxic-to-anoxic transition in the Cariaco Basin, Venezuela. *Chem. Geol.* **195**, 131–157.

Martin C. E., Peucker-Ehrenbrink B., Brunskill G. J. and Szymczak R. (2000) Sources and sinks of unradiogenic osmium runoff from Papua New Guinea. *Earth Planet Sci. Lett.* **183**, 261–274.

Menard H. W. and Smith S. M. (1966) Hypsometry of ocean basin provinces. *J. Geophys. Res.* **71**, 4305–4325.

Middelburg J. J., Soetaert K., Herman P. M. J. and Heip C. H. R. (1996) Denitrification in marine sediments: A model study. *Global Biogeochem. Cy.* **10**, 661–673.

Miller C. A., Peucker-Ehrenbrink B., Walker B. D. and Marcantonio F. (2011) Re-assessing the surface cycling of molybdenum and rhenium. *Geochim. Cosmochim. Acta* **75**, 7146–7179.

Mukherjee I. and Large R. R. (2016) Pyrite trace element chemistry of the Velkerri Formation, Roper Group, McArthur Basin:

Evidence for atmospheric oxygenation during the Boring Billion. *Precambrian Res.* **281**, 13–26.

Mukherjee I., Large R. R., Bull S., Gregory D. G., Stepanov A. S., Ávila J., Ireland T. R. and Corkrey R. (2019) Pyrite trace-element and sulfur isotope geochemistry of paleo-mesoproterozoic McArthur Basin: Proxy for oxidative weathering. *American Mineralogist* **104**, 1256–1272.

Nägler T. F., Anbar A. D., Archer C., Goldberg T., Gordon G. W., Greber N. D., Siebert C., Sohrin Y. and Vance D. (2013) Proposal for an International Molybdenum Isotope Measurement Standard and Data Representation. *Geostand. Geoanal. Res.* **38**, 149–151.

Newby S. M., Owens J. D., Schoepfer S. D. and Algeo T. J. (2021) Transient ocean oxygenation at end-Permian mass extinction onset shown by thallium isotopes. *Nature Geosci.* **14**, 678–683.

Nielsen S. G., Goff M., Hesselbo S. P., Jenkyns H. C., LaRowe D. E. and Lee C.-T.-A. (2011) Thallium isotopes in early diagenetic pyrite – A paleoredox proxy? *Geochim. Cosmochim. Acta* **75**, 6690–6704.

Nielsen S. G., Mar-Gerrison S., Gannoun A., LaRowe D., Klemm V., Halliday A. N., Burton K. W. and Hein J. R. (2009) Thallium isotope evidence for a permanent increase in marine organic carbon export in the early Eocene. *Earth Planet Sci. Lett.* **278**, 297–307.

Nielsen S. G., Rehkämper M., Baker J. and Halliday A. N. (2004) The precise and accurate determination of thallium isotope compositions and concentrations for water samples by MC-ICPMS. *Chem. Geol.* **204**, 109–124.

Nielsen S. G., Rehkamper M., Norman M. D., Halliday A. N. and Harrison D. (2006a) Thallium isotopic evidence for ferromanganese sediments in the mantle source of Hawaiian basalts. *Nature* **439**, 314–317.

Nielsen S. G., Rehkämper M., Porcelli D., Andersson P., Halliday A. N., Swarzenski P. W., Latkoczy C. and Günther D. (2005) Thallium isotope composition of the upper continental crust and rivers—An investigation of the continental sources of dissolved marine thallium. *Geochim. Cosmochim. Acta* **69**, 2007–2019.

Nielsen S. G., Rehkämper M. and Prytulak J. (2017) Investigation and Application of Thallium Isotope Fractionation. *Rev. Mineral. Geochem.* **82**, 759–798.

Nielsen S. G., Rehkämper M., Teagle D. A. H., Butterfield D. A., Alt J. C. and Halliday A. N. (2006b) Hydrothermal fluid fluxes calculated from the isotopic mass balance of thallium in the ocean crust. *Earth Planet Sci. Lett.* **251**, 120–133.

Nielsen S. G., Wasylenki L. E., Rehkämper M., Peacock C. L., Xue Z. and Moon E. M. (2013) Towards an understanding of thallium isotope fractionation during adsorption to manganese oxides. *Geochim. Cosmochim. Acta* **117**, 252–265.

Ostrander C. M., Nielsen S. G., Owens J. D., Kendall B., Gordon G. W., Romaniello S. J. and Anbar A. D. (2019) Fully oxygenated water columns over continental shelves before the Great Oxidation Event. *Nat. Geosci.* **12**, 186–191.

Ostrander C. M., Owens J. D. and Nielsen S. G. (2017) Constraining the rate of oceanic deoxygenation leading up to a Cretaceous Oceanic Anoxic Event (OAE-2: ~94 Ma). *Sci. Adv.* **3** e1701020.

Ostrander C. M., Owens J. D., Nielsen S. G., Lyons T. W., Shu Y., Chen X., Sperling E. A., Jiang G., Johnston D. T. and Sahoo S. K. (2020) Thallium isotope ratios in shales from South China and northwestern Canada suggest widespread O_2 accumulation in marine bottom waters was an uncommon occurrence during the Ediacaran Period. *Chem. Geol.* **557** 119856.

Owens, J.D. (2019) Application of Thallium Isotopes.

Owens J. D., Nielsen S. G., Horner T. J., Ostrander C. M. and Peterson L. C. (2017) Thallium-isotopic compositions of euxinic sediments as a proxy for global manganese-oxide burial. *Geochim. Cosmochim. Acta* **213**, 291–307.

Ozaki K., Reinhard C. T. and Tajika E. (2018) A sluggish mid-Proterozoic biosphere and its effect on Earth's redox balance. *Geobiology* **17**, 3–11.

Page R. W., Jackson M. J. and Krassay A. A. (2000) Constraining sequence stratigraphy in north Australian basins: SHRIMP U-Pb zircon geochronology between Mt Isa and McArthur River*. *Austrian J. Earth Sci.* **47**, 431–459.

Partin C. A., Bekker A., Planavsky N. J., Scott C. T., Gill B. C., Li C., Podkovyrov V., Maslov A., Konhauser K. O., Lalonde S. V., Love G. D., Poulton S. W. and Lyons T. W. (2013) Large-scale fluctuations in Precambrian atmospheric and oceanic oxygen levels from the record of U in shales. *Earth Planet Sci. Lett.* **369–370**, 284–293.

Peacock C. L. and Moon E. M. (2012) Oxidative scavenging of thallium by birnessite: Explanation for thallium enrichment and stable isotope fractionation in marine ferromanganese precipitates. *Geochim. Cosmochim. Acta* **84**, 297–313.

Peucker-Ehrenbrink B. and Hannigan R. E. (2000) Effects of black shale weathering on the mobility of rhenium and platinum group elements. *Geology* **28**, 475–478.

Planavsky N. J., Cole D. B., Reinhard C. T., Diamond C., Love G. D., Luo G., Zhang S., Konhauser K. O. and Lyons T. W. (2016) No evidence for high atmospheric oxygen levels 1,400 million years ago. *Proc. Natl. Acad. Sci. U. S. A.* **113**, E2550–E2551.

Planavsky N. J., McGoldrick P., Scott C. T., Li C., Reinhard C. T., Kelly A. E., Chu X., Bekker A., Love G. D. and Lyons T. W. (2011) Widespread iron-rich conditions in the mid-Proterozoic ocean. *Nature* **477**, 448–451.

Planavsky N. J., Reinhard C. T., Wang X., Thomson D., McGoldrick P., Rainbird R. H., Johnson T., Fischer W. W. and Lyons T. W. (2014) Earth history. Low mid-Proterozoic atmospheric oxygen levels and the delayed rise of animals. *Science* **346**, 635–638.

Polito P. A., Kyser T. K., Southgate P. N. and Jackson M. J. (2006) Sandstone diagenesis in the Mount Isa basin: An isotopic and fluid inclusion perspective in relationship to district-wide Zn, Pb, and Cu mineralization. *Econ. Geol.* **101**, 1159–1188.

Poulton S. W. and Canfield D. E. (2011) Ferruginous Conditions: A Dominant Feature of the Ocean through Earth's History. *Elements.* **7**, 107–112.

Prytulak J., Nielsen S. G., Plank T., Barker M. and Elliott T. (2013) Assessing the utility of thallium and thallium isotopes for tracing subduction zone inputs to the Mariana arc. *Chem. Geol.* **345**, 139–149.

Rader S. T., Mazdab F. K. and Barton M. D. (2018) Mineralogical thallium geochemistry and isotope variations from igneous, metamorphic, and metasomatic systems. *Geochim. Cosmochim. Acta* **243**, 42–65.

Raiswell R. and Anderson T. (2005) Reactive iron enrichment in sediments deposited beneath euxinic bottom waters: constraints on supply by shelf recycling. *Geological Society, London, Special Publications* **248**, 179–194.

Raiswell R., Buckley F., Berner R. A. and Anderson T. (1988) Degree of pyritization of iron as a paleoenvironmental indicator of bottom-water oxygenation. *J. Sediment. Res.* **58**, 812–819.

Raiswell R. and Canfield D. E. (1996) Rates of reaction between silicate iron and dissolved sulfide in Peru Margin sediments. *Geochim. Cosmochim. Acta* **60**, 2777–2787.

Raiswell R. and Canfield D. E. (1998) Sources of iron for pyrite formation in marine sediments. *Amer. J. Sci.* **298**, 219–245.

Raiswell R., Hardisty D. S., Lyons T. W., Canfield D. E., Owens J. D., Planavsky N. J., Poulton S. W. and Reinhard C. T. (2018) The iron paleoredox proxies: A guide to the pitfalls, problems and proper practice. *Amer. J. Sci.* **318**, 491–526.

Ravizza G. and Esser B. (1993) A possible link between the seawater osmium isotope record and weathering of ancient sedimentary organic matter. *Chem. Geol.* **107**, 255–258.

Ravizza G., Turekian K. and Hay B. (1991) The geochemistry of rhenium and osmium in recent sediments from the Black Sea. *Geochim. Cosmochim. Acta* **55**, 3741–3752.

Rawlings D., Korsch R., Goleby B., Gibson G., Johnstone D. and Barlow M. (2004) The 2002 southern McArthur Basin seismic reflection survey. *Geoscience Australia, Record* **17**, 78.

Rehkämper M., Frank M., Hein J. R. and Halliday A. (2004) Cenozoic marine geochemistry of thallium deduced from isotopic studies of ferromanganese crusts and pelagic sediments. *Earth Planet Sci. Lett.* **219**, 77–91.

Rehkämper M., Frank M., Hein J. R., Porcelli D., Halliday A., Ingri J. and Liebetrau V. (2002) Thallium isotope variations in seawater and hydrogenetic, diagenetic, and hydrothermal ferromanganese deposits. *Earth Planet Sci. Lett.* **197**, 65–81.

Rehkämper M. and Halliday A. N. (1999) The precise measurement of Tl isotopic compositions by MC-ICPMS: Application to the analysis of geological materials and meteorites. *Geochim. Cosmochim. Acta* **63**, 935–944.

Rehkämper M. and Nielsen S. G. (2004) The mass balance of dissolved thallium in the oceans. *Mar. Chem.* **85**, 125–139.

Reinhard C. T., Planavsky N. J., Gill B. C., Ozaki K., Robbins L. J., Lyons T. W., Fischer W. W., Wang C., Cole D. B. and Konhauser K. O. (2017) Evolution of the global phosphorus cycle. *Nature* **541**, 386–389.

Reinhard C. T., Planavsky N. J., Olson S. L., Lyons T. W. and Erwin D. H. (2016) Earth's oxygen cycle and the evolution of animal life. *Proc. Natl. Acad. Sci. U. S. A.* **113**, 8933–8938.

Reinhard C. T., Planavsky N. J., Robbins L. J., Partin C. A., Gill B. C., Lalonde S. V., Bekker A., Konhauser K. O. and Lyons T. W. (2013) Proterozoic ocean redox and biogeochemical stasis. *Proc. Natl. Acad. Sci. U. S. A.* **110**, 5357–5362.

Rooney A. D., Chew D. M. and Selby D. (2011) Re–Os geochronology of the Neoproterozoic-Cambrian Dalradian Supergroup of Scotland and Ireland: Implications for Neoproterozoic stratigraphy, glaciations and Re–Os systematics. *Precambrian Res.* **185**, 202–214.

Schoenberg R., Zink S., Staubwasser M. and von Blanckenburg F. (2008) The stable Cr isotope inventory of solid Earth reservoirs determined by double spike MC-ICP-MS. *Chem. Geol.* **249**, 294–306.

Scott C., Lyons T. W., Bekker A., Shen Y., Poulton S. W., Chu X. and Anbar A. D. (2008) Tracing the stepwise oxygenation of the Proterozoic ocean. *Nature* **452**, 456–459.

Selby D. and Creaser R. A. (2003) Re–Os geochronology of organic rich sediments: an evaluation of organic matter analysis methods. *Chem. Geol.* **200**, 225–240.

Selby D., Creaser R. A., Stein H. J., Markey R. J. and Hannah J. L. (2007) Assessment of the ^{187}Re decay constant by cross calibration of Re–Os molybdenite and U-Pb zircon chronometers in magmatic ore systems. *Geochim. Cosmochim. Acta* **71**, 1999–2013.

Sheen A. I., Kendall B., Reinhard C. T., Creaser R. A., Lyons T. W., Bekker A., Poulton S. W. and Anbar A. D. (2018) A model for the oceanic mass balance of rhenium and implications for the extent of Proterozoic ocean anoxia. *Geochim. Cosmochim. Acta* **227**, 75–95.

Shen Y. (2002) Middle Proterozoic ocean chemistry: Evidence from the McArthur Basin, northern Australia. *Amer. J. Sci.* **302**, 81–109.

Shen Y., Knoll A. H. and Walter M. R. (2003) Evidence for low sulphate and anoxia in a mid-Proterozoic marine basin. *Nature* **423**, 632–635.

Slack J. F., Grenne T., Bekker A., Rouxel O. J. and Lindberg P. A. (2007) Suboxic deep seawater in the late Paleoproterozoic: Evidence from hematitic chert and iron formation related to seafloor-hydrothermal sulfide deposits, central Arizona, USA. *Earth Planet Sci. Lett.* **255**, 243–256.

Smoliar M. I., Walker R. J. and Morgan J. W. (1996) Re-Os ages of group IIA, IIIA, IVA, and IVB iron meteorites. *Science* **271**, 1099–1102.

Soetaert K. E., Petzoldt T. and Setzer R. W. (2010) Solving differential equations in R: package deSolve. *J. stat. softw.* **33**, 1–25.

Southgate P. N., Bradshaw B. E., Domagala J., Jackson M. J., Idnurm M., Krassay A. A., Page R. W., Sami T. T., Scott D. L., Lindsay J. F., McConachie B. A. and Tarlowski C. (2000) Chronostratigraphic basin framework for Palaeoproterozoic rocks (1730–1575 Ma) in northern Australia and implications for base-metal mineralisation. *Austrian J. Earth Sci.* **47**, 461–483.

Sperling E. A., Rooney A. D., Hays L., Sergeev V. N., Vorob'eva N. G., Sergeeva N. D., Selby D., Johnston D. T. and Knoll A. H. (2014) Redox heterogeneity of subsurface waters in the Mesoproterozoic ocean. *Geobiology* **12**, 373–386.

Sperling E. A., Wolock C. J., Morgan A. S., Gill B. C., Kunzmann M., Halverson G. P., Macdonald F. A., Knoll A. H. and Johnston D. T. (2015) Statistical analysis of iron geochemical data suggests limited late Proterozoic oxygenation. *Nature* **523**, 451–454.

Spinks S. C., Pearce M. A., Liu W., Kunzmann M., Ryan C. G., Moorhead G. F., Kirkham R., Blaikie T., Sheldon H. A. and Schaubs P. M. (2021) Carbonate Replacement as the Principal Ore Formation Process in the Proterozoic McArthur River (HYC) Sediment-Hosted Zn-Pb Deposit, Australia. *Econ. Geol.* **116**, 693–718.

Spinks S. C., Schmid S., Pagés A. and Bluett J. (2016) Evidence for SEDEX-style mineralization in the 1.7 Ga Tawallah Group, McArthur Basin, Australia. *Ore Geol. Rev.* **76**, 122–139.

Stockey R. G., Cole D. B., Planavsky N. J., Loydell D. K., Fryda J. and Sperling E. A. (2020) Persistent global marine euxinia in the early Silurian. *Nat. Commun.* **11**, 1804.

Stolper D. A. and Keller C. B. (2018) A record of deep-ocean dissolved O_2 from the oxidation state of iron in submarine basalts. *Nature* **553**, 323–327.

Symons D. (2007) Paleomagnetism of the HYC Zn-Pb SEDEX Deposit, Australia: evidence of an epigenetic origin. *Econ. Geol.* **102**, 1295–1310.

Tang D., Shi X., Wang X. and Jiang G. (2016a) Extremely low oxygen concentration in mid-Proterozoic shallow seawaters. *Precambrian Res.* **276**, 145–157.

Tang M., Chen K. and Rudnick R. L. (2016b) Archean upper crust transition from mafic to felsic marks the onset of plate tectonics. *Science* **351**, 372–375.

Them T. R., Gill B. C., Caruthers A. H., Gerhardt A. M., Grocke D. R., Lyons T. W., Marroquin S. M., Nielsen S. G., Trabucho Alexandre J. P. and Owens J. D. (2018) Thallium isotopes reveal protracted anoxia during the Toarcian (Early Jurassic) associated with volcanism, carbon burial, and mass extinction. *Proc. Natl. Acad. Sci. U. S. A.* **115**, 6596–6601.

Vinnichenko G., Jarrett A. J., Hope J. M. and Brocks J. J. (2020) Discovery of the oldest known biomarkers provides evidence for phototrophic bacteria in the 1.73 Ga Wollogorang Formation, Australia. *Geobiology* **18**, 544–559.

Volk H., George S. C., Dutkiewicz A. and Ridley J. (2005) Characterisation of fluid inclusion oil in a Mid-Proterozoic

sandstone and dolerite (Roper Superbasin, Australia). *Chem. Geol.* **223**, 109–135.

Wang H., Zhang Z., Li C., Algeo T. J., Cheng M. and Wang W. (2020) Spatiotemporal redox heterogeneity and transient marine shelf oxygenation in the Mesoproterozoic ocean. *Geochimica et Cosmochimica Acta* **270**, 201–217.

Warren J. K., George S. C., Hamilton P. J. and Tingate P. (1998) Proterozoic Source Rocks: Sedimentology and Organic Characteristics of the Velkerri Formation, Northern Territory, Australia1. *AAPG Bull.* **82**, 442–463.

Wijsman J. W., Middelburg J. J. and Heip C. H. (2001) Reactive iron in Black Sea sediments: implications for iron cycling. *Mar. Geol.* **172**, 167–180.

Williford K. H., Van Kranendonk M. J., Ushikubo T., Kozdon R. and Valley J. W. (2011) Constraining atmospheric oxygen and seawater sulfate concentrations during Paleoproterozoic glaciation: In situ sulfur three-isotope microanalysis of pyrite from the Turee Creek Group, Western Australia. *Geochim. Cosmochim. Acta* **75**, 5686–5705.

Yang B., Collins A., Blades M., Capogreco N., Payne J., Munson T., Cox G. and Glorie S. (2019) Middle–late Mesoproterozoic tectonic geography of the North Australia Craton: U-Pb and Hf isotopes of detrital zircon grains in the Beetaloo Sub-basin, Northern Territory, Australia. *J. Geol. Soc.* **176**, 771–784.

Yang B., Smith T. M., Collins A. S., Munson T. J., Schoemaker B., Nicholls D., Cox G., Farkas J. and Glorie S. (2018) Spatial and temporal variation in detrital zircon age provenance of the hydrocarbon-bearing upper Roper Group, Beetaloo Sub-basin, Northern Territory, Australia. *Precambrian Res.* **304**, 140–155.

Yang S., Kendall B., Lu X., Zhang F. and Zheng W. (2017) Uranium isotope compositions of mid-Proterozoic black shales: Evidence for an episode of increased ocean oxygenation at 1.36 Ga and evaluation of the effect of post-depositional hydrothermal fluid flow. *Precambrian Res.* **298**, 187–201.

Zhang S., Wang X., Wang H., Bjerrum C. J., Hammarlund E. U., Costa M. M., Connelly J. N., Zhang B., Su J. and Canfield D. E. (2016) Sufficient oxygen for animal respiration 1,400 million years ago. *Proc. Natl. Acad. Sci. U. S. A.* **113**, 1731–1736.

Zhang S., Wang X., Wang H., Bjerrum C. J., Hammarlund E. U., Haxen E. R., Wen H., Ye Y. and Canfield D. E. (2019) Paleoenvironmental proxies and what the Xiamaling Formation tells us about the mid-Proterozoic ocean. *Geobiol.* **17**, 225–246.

Associate editor: Susan Halsall Little